Design of an Ultra-Wide Band based Indoor Positioning System

DESIGN OF AN ULTRA-WIDE BAND BASED INDOOR POSITIONING SYSTEM

BY

JUN LI, M.Sc., (Electrical Engineering)

Huazhong University of Science and Technology, Wuhan, China

A THESIS

SUBMITTED TO THE DEPARTMENT OF COMPUTING AND SOFTWARE

AND THE SCHOOL OF GRADUATE STUDIES

OF MCMASTER UNIVERSITY

IN PARTIAL FULFILMENT OF THE REQUIREMENTS

FOR THE DEGREE OF

MASTER OF SCIENCE

Master of Science (2018)	McMaster University
(Computing and Software)	Hamilton, Ontario, Canada

TITLE:	Design of an Ultra-Wide Band based Indoor Positioning System
AUTHOR:	Jun Li M.Sc., (Electrical Engineering) Huazhong University of Science and Technology, Wuhan, China
SUPERVISOR:	Dr. Rong Zheng
NUMBER OF PAGES:	xvi, 78

Abstract

In recent years, indoor positioning system (IPS) has attracted significant interests in both academical research and industrial development. It has seen many applications, such as hostage search and rescue, indoor navigation, and warehouse management, all of which can take advantage of precise positioning. However, in indoor environments, traditional methods, like the Global Positioning System (GPS), are usually either unreliable or incorrect because of the complicated physical characteristics of various objects reflecting and dispersing signals, such as the presence of people, walls, obstructions, and furniture. In contrast to other technologies such as WiFi and Bluetooth, which are not suitable to extract accurate timing information, UWB technology has the potential to reach center-meter level accuracy in indoor positioning. In this thesis, we developed a real-time, low-cost, IPS based on commercial-off-the-shelf UWB transceivers. Both the Two Way Ranging (TWR) and Time Difference of Arrival (TDOA) approaches have been implemented to obtain a target's location. To alleviate the effect of multipath propagation, we detect the presence of outliers by comparing the first path signal level and estimated receiving signal level. Moreover, we have designed the Printed Circuit Board (PCB) and evaluated performance by deploying the system both in a lab environment and in a two-story historical building during the 2018 Microsoft Indoor Localization Competition. The results show that we achieve a 28.9cm 95%-quantile 2D tracking error in the lab environment and a 92cm average tracking error for 3D localization on the Microsoft Indoor Localization Competition site.

Acknowledgements

It has been an unforgettable experience to study in the Wireless System Research group. We have had a lot of interesting projects, and outstanding ideas sparked among us quite often. I have been in charge of hardware support for the group, and thus have the opportunities to collaborate with almost all the team members who have also become my best friends. I enjoyed the time working with Yuting Wang on his asynchronous acoustic indoor positioning system, which brought me into the field of indoor localization. All the nights working overtime in preparation for international localization competitions seem like yesterday and were a rewarding experience. I will not forget Ala, a handsome guy who always invited me for coffee. Also, along with the strongest man, Cristian, the deep learning mentor, Yihap, and the IPS expert Qiang, we have all work together through exciting and stressful periods with fun and love.

I would like to thank my supervisor Dr. Rong Zheng for giving me a chance to study at the McMaster University and providing me with a scholarship. She is a brilliant academic who always helped us solve problems we encountered in our research. Her ability to break down sophisticated issues into small pieces and lead us to think and solve them by ourselves was particularly helpful. Her advice and suggestions were incredibly valuable, and often showed us the path forward.

I would like to offer my special thanks to Chenhe Li, with whom I worked for two years and tackled numerous problems. He is a great friend and competent partner. No matter what our firmware issues were, he had hundreds of methods to fix them. He regularly guided me through learning programming and coding skills. No words is sufficient to express my appreciation.

Most importantly, I would like to express my sincere gratitude to my wife, Juanjuan He. Without her selfless support and understanding, I would not be able to come this far.

Abbreviations

GPS	Global Positioning System
IPS	Indoor Positioning System
UWB	Ultra-Wide Band
PCB	Printed Circuit Board
TWR	Two-Way Ranging
LOS	Line of Sight
NLOS	Non-Line of Sight
WLAN	Wireless Local Area Network
LBS	Location-based Services (LBS)
TOA	Time of Arrival
TDOA	Time Difference of Arrival
PDR	Pedestrian Dead Reckoning
RSSI	Received Signal Strength Indication
BLE	Bluetooth Low Energy
IMU	Inertial Measurement Unit
FCC	Federal Communications Commission
RF	Radio Frequency

EIRP	Equivalent Isotropically Radiated Power
DS-TWR	Double Side Two-Way Ranging
LS	Least Square
RMSE	Root Mean Square Error
PF	Particle Filter
EKF	Extend Kalman Filter
VIO	Visual-Inertial Odometry
RTLS	Real Time Location System
1D	One-Dimensional
2D	Two-Dimensional
3D	Three-Dimensional
SS-TWR	Single Sided TWR
DS-TWR	Double sided TWR
RSS	Receiving Signal Strength
TMDS-TWR	Three messages DS-TWR
PPM	Part Per Million
SDK	Software Development Kit
DC	Direct Current
PHY	Physical Layer
SHR	Synchronization Header
SFD	Start of Frame Delimiter
PRF	Pulse Repetition Frequencies
API	Application Programming Interface
CDF	Cumulative Distribution Function

Contents

List of Figures

List of Tables

Chapter 1

Introduction

1.1 Indoor Positioning

Positioning, by definition, is to determine where an event occurs or where an object or a person locates. The development of positioning technologies has had profound impacts on people's daily lives in recent years. It brings convenience to travel, navigation, and makes people more mobile. Moreover, location information can be used to analyze human behavior in medical fields. Accordingly, location-based services (LBS), which built upon precise positioning information, have become an growing market and are attracting much interest from both research and industry.

According to the environment in which LBS are applied, positioning can be classified into two types, outdoor positioning and indoor positioning. Different kinds of positioning technologies can be employed depending the application requirements and constraints. In outdoor environments, location information can be easily obtained by means of GPS with a global average user range error of $7.8m$ with 95% Confidence Interval, claimed by United States government in 2017 [7]. GPS receivers have become ubiquitous in mobile devices as an industrial standard configuration. The GPS technology utilizes ultra high precision atomic clocks to measure the Time of Arrival (TOA) among GPS satellites and user. With at least four TOA timings and the radius of earth, the user's positioning and local time offset can be determined via a trilateration algorithm [8]. However, GPS becomes unreliable or unusable in indoor environments. On one hand, even if satellite radio signals manage to penetrate walls and obstacles, those signals attenuate dramatically, leading to degraded performance. On the other hand, multipath effects and absence of a Line of Sight (LOS) path also mean that GPS signals cannot travel directly in the straight path from the transmitter to the receiver (Fig. 1.1) [9]. In LOS conditions (Fig. 1.1a), the direct path signal could be detected and received in spite of the obstacle existing between the transmitter and receiver(Fig. 1.1c). However, in Non-Line of Sight (NLOS) conditions, only the reflection signal can be received resulting incorrect estimation of propagation paths (Fig. 1.1d).

Compared to outdoor conditions, indoor environments are more difficult to obtain a location within, since the complex physical characteristics of indoor environments and the presence of people, walls, obstructions, and furniture regularly cause severe reflection, attenuation of signals, and multipath propagation [10]. In addition, indoor positioning typically demands a sub-meter-level positioning accuracy. Indeed, accurate position results are crucial for indoor LBS such as inventory tracking, indoor navigation, industrial control, indoor flow analysis in retail businesses and events, etc.. For example, an IPS with 3-meter error may wrongly guide a visually impair person to a stairway as opposed to an elevator.

Over the past decade, many approaches have been developed for IPS [11, 12,

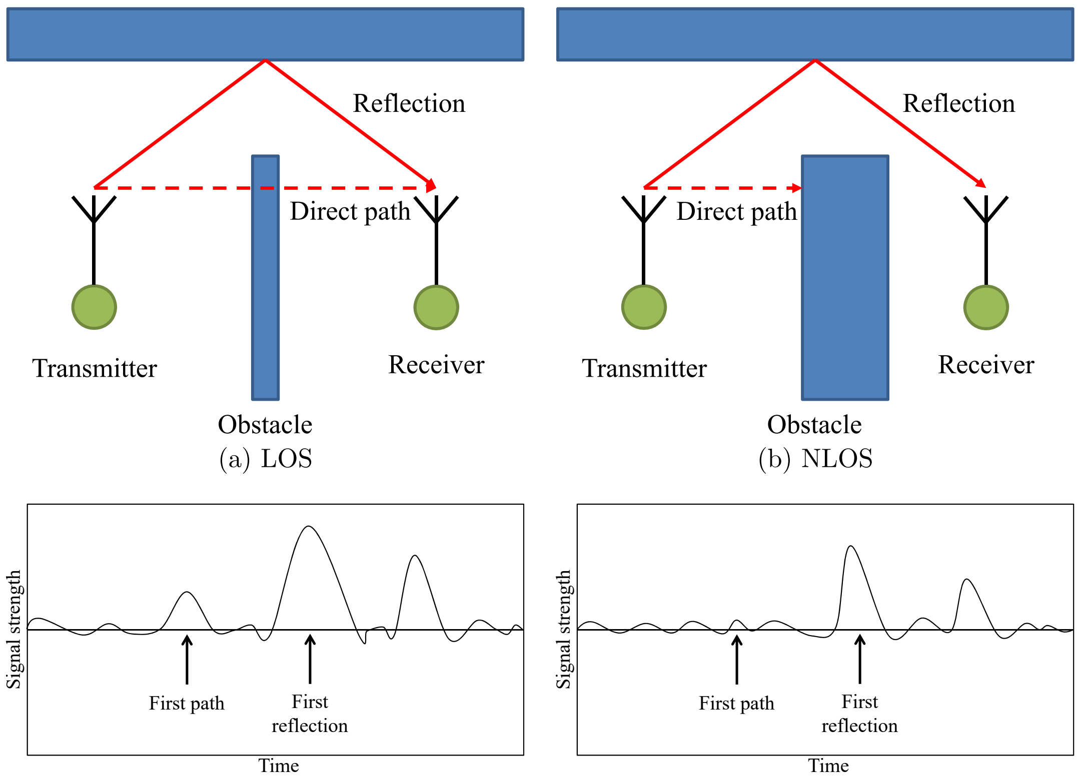

(a) LOS (b) NLOS

(c) Channel impulse response view for LOS (d) Channel impulse response view for NLOS

Figure 1.1: Illustration of LOS and NLOS scenarios

13, 14]. For example, fingerprinting and Pedestrian Dead Reckoning (PDR) are two common solutions in infrastructure-free IPS scenarios, which means these IPS only leverage existing resource and do not need to deploy other equipments or objects for estimating locations. Fingerprinting utilizes received wireless signal strength, also known as the Received Signal Strength Indication (RSSI), to estimate the locations of targets. It reduces deployment costs by relying on existing network infrastructure, such as WiFi, Bluetooth Low Energy (BLE), and Zigbee.

However, a radio strength map, also known as fingerprints, needs to be created before one can use an RSSI based IPS. As Fig. 1.2 shows, the RSSI information with

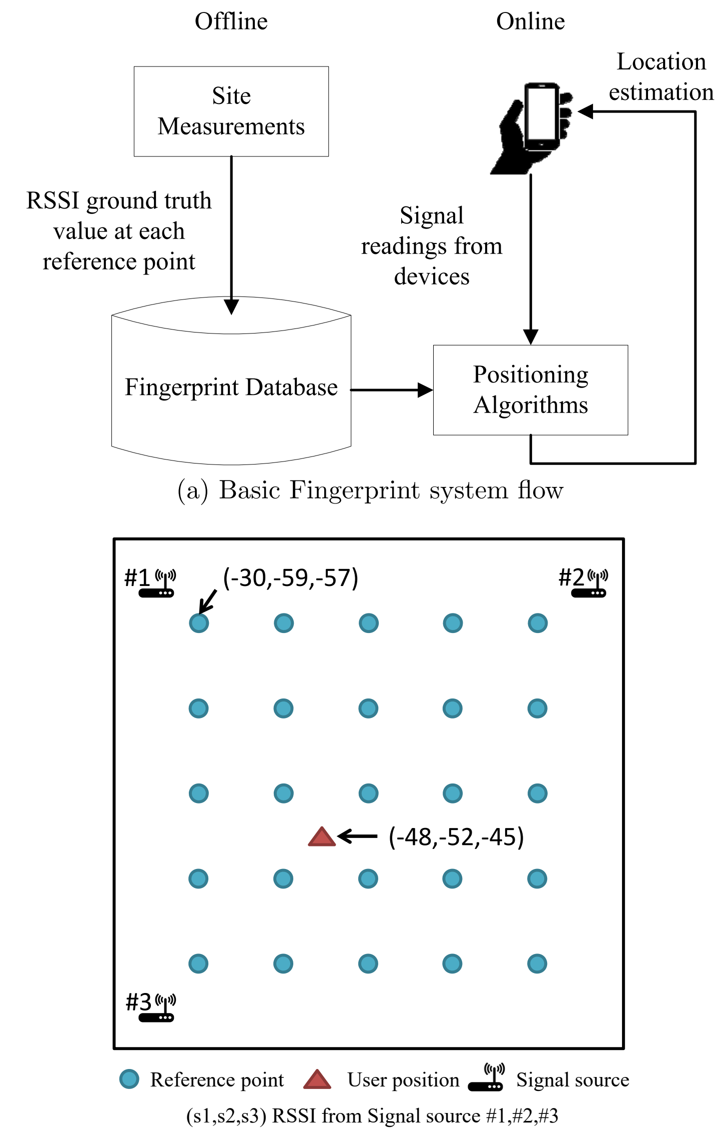

(a) Basic Fingerprint system flow

(b) RSSI map

Figure 1.2: Illustration of fingerprinting-based approach

respect to each fixed transmitter at all reference locations needs to be collected to construct a fingerprint database or to train a regression model. Once mobile devices measure the RSSI from each fixed transmitter, the system compares the measurements with the fingerprint map and estimates the the devices' location. Generating a radio strength map requires survey of the entire indoor space, which is labor intensive. Furthermore, the fingerprint database needs frequent updates because of changes in indoor environments. As a direct result, this approach can achieve about 1 to $3m$ accuracy [14].

PDR utilizes inertial measurement units (IMU) on cellphones or wearable devices to estimate pedestrian locations. PDR works well within short distances or in constrained environment [15]. The main drawback of PDR is that the positioning error accumulates over time and thus absolute position calibration is needed from time to time.

Beside RF fingerprinting-based methods and PDR, time-domain approaches that estimate the TOA and TDOA have been investigated. However, due to stringent timing requirements, they are generally not suitable for implementation on narrow-band radios. There are ongoing efforts on developing time-domain methods using acoustic signals [16] and ultra-wide band radios, the focus of the thesis.

1.2 Ultra-Wide Band Technology

In the United States, the Federal Communications Commission (FCC) defines UWB as a Radio Frequency (RF) signal wherein either the bandwidth of the signal is greater than $500MHz$ or 20% of the center frequency. It can be presented with 1.1 and 1.2, where B is the bandwidth, B_f is the fractional bandwidth which represent the fraction of the bandwidth divided by its center frequency, f_H is the upper frequency of the -10dB down point and f_L is the lower frequency of the -10dB down point (Fig. 1.3). FCC regulations cover three classes of devices: imaging systems, vehicular radar systems, and communications and measurement systems. UWB-based IPS belongs to communications and measurement systems, and must satisfy emission limitations: (1) the operating band needs to be between 3.1 and 10.6GHz; and (2) the average measured equivalent isotropically radiated power (EIRP) should be less than -41.3dBm in any 1MHz signal bandwidth [17].

$$B = f_H - f_l \geq 500MHz \tag{1.1}$$

or

$$B_f = 2 \times \frac{B}{f_H + f_l} \geq 0.2 \tag{1.2}$$

In general, UWB has different features compared to narrow-band or broad-band wireless signals. Specifically, its radio pulses are extremely short and occupy a wide frequency band. The ultra-short UWB pulses make the signal pass through obstacles effectively and reduce multipath effects resulting in fine time resolution. The high bandwidth provides high data rates for communication. As a result, UWB can provide centimeter level positioning accuracy and can co-exist with existing RF signals or external noise like WiFi and BLE. Furthermore, with the IEEE 802.15.4a standard, the cost of UWB chips has dropped to around $10 USD. Therefore, UWB is a promising choice for indoor positioning applications that require high accuracy. However, UWB signals attenuate significantly when penetrating metallic and liquid materials. Short communication ranges when transmitting at a high data rate limit

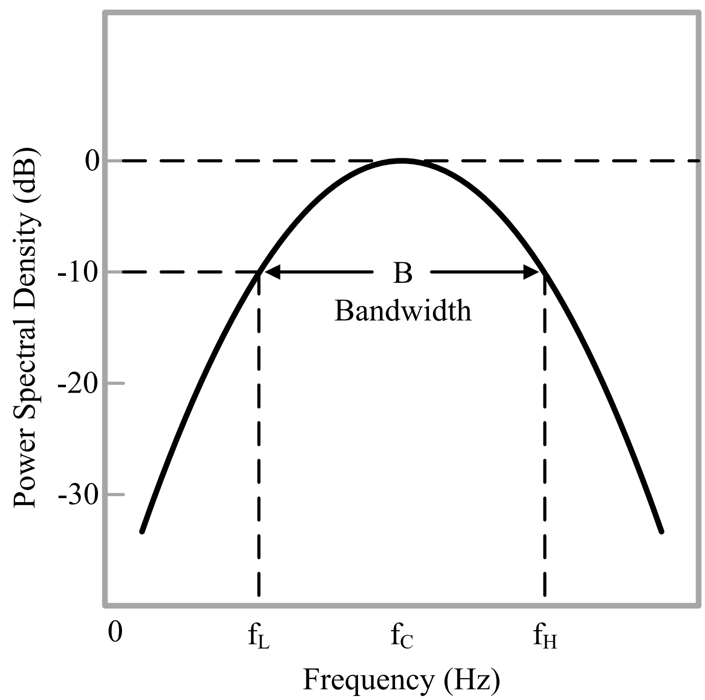

Figure 1.3: FCC UWB Definition

its applications.

1.3 Challenges and Contributions

Although the UWB technology has many advantages, it still faces a number of challenges when employed in indoor positioning applications.

The first challenge is the design of UWB antennas. UWB antennas have to provide a constant gain over the entire operating bandwidth so that the pulse shape is not too distorted to affect accuracy. The design of reliable wide band antennas is challenging. Although UWB has a strong penetration ability, experiments demonstrate that reflection, diffusion, and other propagation effects can distort the pulse shape, consequently affecting ranging accuracy [18]. In this thesis, we will not analyze antenna performance or discuss how to improve the antenna performance, because the UWB module we selected has a PCB antenna. However, we discuss the delay caused by the signal path and PCB antenna in Chapter 4.

The second challenge is policies and regulations UWB use. Several countries have allowed the use of unlicensed spectrum for UWB communication, including the United States, the European Union, and many Asia-Pacific countries. However, the unlicensed spectrum and usage scenarios differ in different countries, thereby impeding the wider adoption of UWB-based applications. Table 1.1 summarizes limitations in different countries/regions [10].

Our main contributions in this thesis lie in three aspects. First, we developed a low-cost and real-time UWB-based IPS prototype for laboratory use. Commercial off-the-shelf UWB-based IPS cost excess of 1000 CAD. For example, the evaluation board from Decawave, EVK1000, is 841.62 CAD and it only contains 2 devices. However, the cost for our design is only around 150 CAD per unit. Second, we have successfully implemented both TWR and TDOA approaches on our prototype platform in a lab environment. Third, to mitigate the effects of low SNR and multi-path propagation, we have devised a robust algorithm that removes possible outliers by taking advantage of receiving signal power difference. Experiments have been carried in two testbeds presented in Section 6.2, one was in an academic building on the McMaster University campus and the other one was in a historical building in Portugal during the 2018 Microsoft Indoor Localization Competition.

The rest of the thesis is organized as follows. Chapter 2 reviews the related work on UWB-based IPS. Chapter 3 presents an overview of the proposed UWB-based IPS. We discuss the sources of errors in UWB-based IPS in Chapter 4. In Chapter 5,

Table 1.1: UWB limitations in different countries

Country	**License**	**Spectrum Range**	**Limitations**
U.S.	Unlicensed	3.1 GHz to 10.6 GHz	Indoor only
European Union	Unlicensed	3.1 GHz to 10.6 GHz	Indoor only
United Kingdom	Unlicensed	3.1 GHz to 10.6 GHz	Indoor/Outdoor
Japan	Unlicensed	3.4 GHz to 10.25 GHz	Indoor only
Singapore	Unlicensed	3.4 GHz to 9 GHz	Indoor only

we present the details of the software and hardware implementation, followed by performance evaluation in Chapter 6. Finally, we summarize the thesis and discuss future work in Chapter 7.

Chapter 2

Related Work

According to the United States national human activity pattern survey, people spent approximately 87% of their time indoors [19]. The market research survey from Technavio forecasts that the global indoor LBS market will grow at a compound annual growth rate of more than 43% over the next five years [20]. IPS has attracted numerous interests from both academic researchers and industrial investors. Various indoor positioning technologies have been studied and used. They can be classified as (1) infrared technologies; (2) ultra-sound technologies; (3) RF technologies (which UWB technology belongs to); (4) magnetic technologies; (5) vision-based technologies; and (6) audible and near-ultra sound technologies. In this chapter, we focus on UWB-based IPS approaches. First, we introduce the mainstream research and commercial solutions. Next, we present time-domain location approaches and NLOS detection mechanisms. Comprehensive surveys of related work in this field can be found in [10, 11, 13, 21].

2.1 Research on UWB-based IPS

In recent years, UWB-based IPS has gained much interest due to availability of low-cost hardware. Low et al. [22] achieved centimeter-range accuracy in a one-dimensional (1D) indoor LOS environment utilizing the TOA of UWB pulse signals. The signals were generated and received by a signal generator and spectrum analyzer. The mean location errors were $0.503cm$ at $7.4m$ distance and $1.677cm$ at $24m$ distance. González et al. [23] showed navigation results for a robot moving in indoor scenarios covered by three UWB beacons to evaluate UWB ranges in both LOS and NLOS conditions by PulsOn kits, commercialized by Time Domain [24]. Within a $13m \times 10m$ room where three fixed UWB beacons were placed at known positions, testers have achieved under $5cm$ and $1.5m$ two-dimensional (2D) average error for LOS and NLOS configurations respectively. To improve the performance in NLOS scenarios, Geng et al. [25] and He et al. [26] studied and introduced TOA ranging error models for body mounted sensors based on real measurements. Those models separated the ranging errors into errors from multiple effects and NLOS, caused by the signal penetrating human body. Combined with IMUs or visual sensors, UWB can overcome the limitations of either technology alone. Tiemann et al. [27, 28] and Fresk et al. [29] presented novel applications with autonomous Unmanned Aerial Vehicle (UAV) systems, which used IMUs provide location informations for UAV, and utilized UWB location measurements to mitigate the IMU errors from IMU. Tiemann et al. deployed 8 UWB anchor nodes within a $3.6m \times 1.2m$ space in the LOS condition, and adopted a TDOA approach to calibrate the IMU data. The 95%-quantile 2D and three-dimensional (3D) localization errors are about $0.15m$ and $0.34m$ respectively. Fresk et al. adopted a Two-Way Ranging (TWR) approach for localization

Table 2.1: Comparison of related works.

Related Work	**Approach**	**Testbed size**	**Error**	**Comment**
Low et al. [22]	TOA	$7.4m$ $24m$	$0.503cm$ $1.677cm$	1D, mean error, LOS 1D, mean error, LOS
LGonzález et al. [23]	TWR	$13m \times 10m$	$4.7cm$ $1.5m$	2D, LOS, 3 anchors, PF 2D, NLOS, 3 anchors, PF
Tiemann et al. [27, 28]	TDOA, IMUs	$3.6m \times 1.2m$	$15cm$ $34cm$	2D, 95%-quantile error, LOS, 8 anchors 3D, 95%-quantile error, LOS, 8 anchors
Fresk et al. [29]	TWR, IMUs	$5m \times 5m$ $\times 2.8m$	$8.1cm$ $8.2cm$ $6.1cm$	X axis, RMSE, 4 anchors Y axis, RMSE, 4 anchors Z axis, RMSE, 4 anchors
Rajagopal and Miller et al. [30, 31]	TWR, VIO	$15m \times 15m$ $\times 10m$	$27cm$	3D, 10 anchors, Real-time tracking, PF and EKF

using UWB and deployed 4 anchor nodes within a $5m \times 5m \times 2.8m$ flying volume in LOS condition. The root mean square errors (RMSE) for all experiments at X, Y and Z axis are $8.1cm$, $8.2cm$, $6.1cm$. In another interested work by Rajagopal and Miller et al. [30, 31], the authors developed an IPS for mobile devices based on fusion of UWB TOA ranging and visual-inertial odometry (VIO) provided by Apple's ARKit. ARKit generates relative location updates by fusing motion estimations from the camera with IMU readings from a smart phone; while UWB provided the global coordinate reference. Lastly, the phone computes location estimations using Particle Filter (PF) and Extend Kalman Filter (EKF). The system won the first place in Microsoft Indoor Localization Competition 2018 with an 0.27 m average error for 3D localization.

A comparison of selected related works is summarized in Table 2.1.

2.2 Commercial Solutions

There are a number of commercial IPS using UWB in the market, including Ubisense, Alereon, Decawave, Time Domain and Pulse−Link.

Ubisense is one of these well-known providers. The Ubisense UWB positioning systems consist of several anchor nodes deployed at known positions, and tags carried by user has to be located. The anchor nodes leverage the UWB signals from tags to determine the user's positions via TDOA [32]. Real-time location information is used by to manufacturers to maintain continuous flow, reduce errors and improve efficiency in assembly processes. It has been successfully adopted by BMW in its facility in Germany [33].

Alereon provides UWB-based solution to defense contractors and government agencies. Alereon's UWB positioning systems have been used in the U.S. military and customer products [34, 35].

Decawave Ltd. [36] is a UWB chipset and solution vendor. It produces semiconductor chips and modules, software and real-time, accurate and reliable reference designs to customers. Due to its user-friendly UWB modules and comprehensive libraries and application programming interface, we choose Decawave modules in our proposed solution.

A new start-up company named BeSpoon demonstrates smart phones called SpoonPhone with UWB chips inside that do not interfere with the normal usage of smart phones. This integration creates many of useful applications, such as locating one's phone in the house, providing an extra wireless communication interface when WiFi and Bluetooth are unavailable, as well as enabling IPS service [37].

However, Jiménez et al. [38] shows that the performance of the Decawave system (TREK1000) is slightly better in LOS conditions and more reliable in NLOS than the BeSpoon system (SpoonPhone and tags). In addition, Antonio et al. [39] presents a comparison among Ubisense (Ubisense series 7000), BeSpoon (SpoonPhone and tag) and Decawave (TREK1000) location systems. The testbed is of size $24m \times 14m$, a total of 70 test points are selected to evaluate these systems performance, including LOS and NLOS scenarios. The 3D CDF positioning errors has been presented and Decawave achieved highest positioning accuracy.

Time Domain's PulsON products allow researchers and developers to evaluate UWB for ranging, communications, and target tracking. Their latest P440 and P330 modules represent state of the art solutions to UWB precision ranging, localization, and communications [24]. UWB chips used in their products are from Decawave.

Pulse−Link developed a UWB technology based on continuous pulsed UWB for high data rate communication networks. The core of the PL3100 family consists of a PL3120 UWB transceiver and a PL3130 baseband components. The system is specifically designed to provide a highly adaptive protocol and waveforms for various applications and environments [40].

We summarize all the companies' products and software supports in Table 2.2.

2.3 Principles of Time-domain Location Approaches

Time domain positioning approaches require accurately measuring the signal propagation time from a transmitter to a target receiver. Then main stream approaches are presented in this section.

Table 2.2: UWB companies' products and software supports

Company	Chip	Module	Evaluation Kit	Software Development Kit
Ubisense	None	None	Dimension4	Yes
Alereon	AL5100, AL5350	None	AL57600−EVK	Yes
Decawave Ltd.	DW1000	DWM1000, DW1001	EVK1000, TREK1000	Yes
BeSpoon	None	None	SpoonPhone and tags	Yes
Time Domain	None	P330 and P440	None	Yes
Pulse−Link	PL3120, PL3130	None	None	Yes

2.3.1 Time of Arrival

In the simplest conditions, in which the transmitter and the receiver share a common clock, TOA can be calculated by subtracting the sending time recorded by the transmitter from the receiving time recorded by the receiver. One can then estimate the distance by multiplying the TOA with the speed of light [41]. If one of the nodes is in a known position, referred to as a reference node, the node with unknown location, also called the target, falls on a circle (in 2D) that centers at the reference node with the estimated distance as the radius. The distance in 2D between target and reference node i is represented by

$$d_i = \sqrt{(x - x_i)^2 + (y - y_i)^2},\ i = 1, 2, 3.., \tag{2.1}$$

where $(x,\, y)$ is the coordinates of the target and $(x_i,\, y_i)$ are the coordinates of the reference node i. Therefore, in the absence of noise and measurement errors (Fig.2.1), the target can be uniquely localized at the intersecting point of three circles. Similarly, in 3D, at least intersecting four spheres (and consequently 4 reference nodes) are

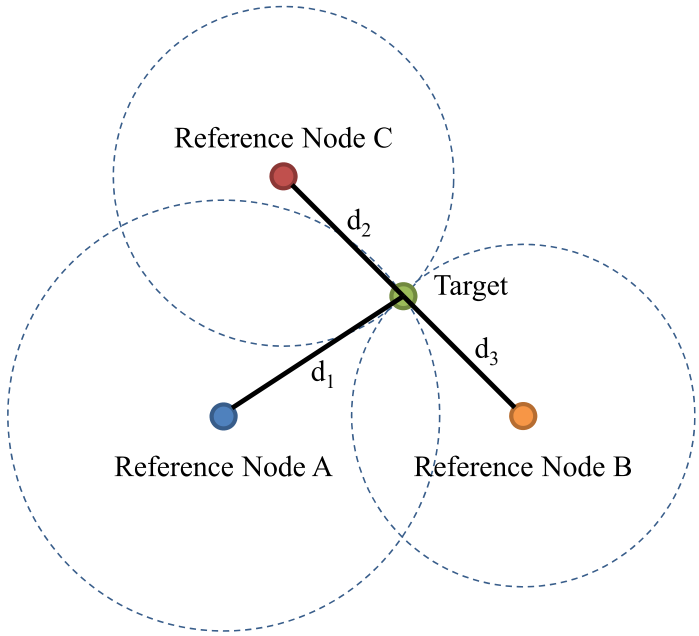

Figure 2.1: TOA position estimation

required to determine a target's position. This method is also known as trilateration.

2.3.2 Time Difference of Arrival

If there is no common clock between the reference nodes and targets, the TDOA approach can be applied as long as tight synchronization can be achieved among the reference nodes. [41]. As shown in Fig. 2.2, upon receiving a signal from a target device, the TDOA of the signal from the target to reference node A and B can be estimated. In absence of noise and measurement errors, the possible positions of target reside on a hyperbola specified by,

$$\begin{aligned} t_{ab}^{TDOA} \times C &= d_1 - d_2 = d_3 - d_4 \\ &= \sqrt{(x-x_a)^2 + (y-y_a)^2} - \sqrt{(x-x_b)^2 + (y-y_b)^2}, \end{aligned} \tag{2.2}$$

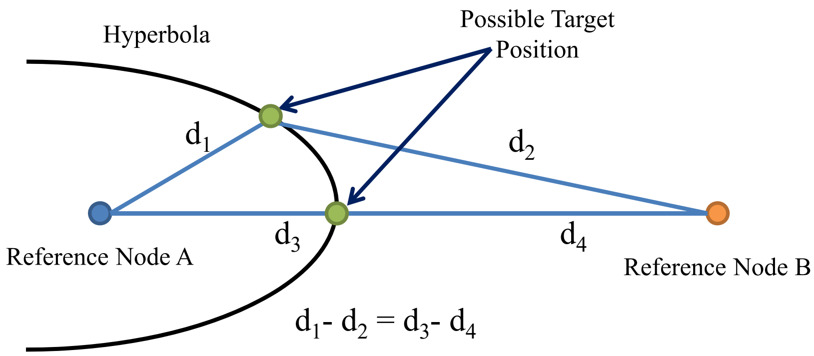

Figure 2.2: TDOA position estimation

where, t_{ab}^{TDOA} represents the TDOA between reference node a and b, C represents the speed of light, (x, y) are the coordinates of the target, $(x_a,\ y_a)$ and $(x_b,\ y_b)$ are the coordinates of reference node a and node b, respectively. At least four (five) reference nodes are needed to uniquely determine the target location in 2D (3D). The main challenge of TDOA-based approaches is the need for precise synchronization among reference nodes. For instance, a timing error of 1 nanosecond is equivalent to a 30 cm distance error. However, TDOA-based approaches are advantageous in that only one message transmission is needed from a target device resulting high power efficiency. Moreover, with more reference nodes in the target's vicinity, location estimation accuracy can be improved.

2.3.3 Two-Way Ranging

With no common clock among reference nodes, the distance between a reference node and a target can be estimated by the two-way-ranging technique. As the name suggests, TWR technique utilizes bidirectional messages exchanged between a target and a reference node. TWR calculates the distance between the node pair using the time elapse from transmitting a message to receiving its response.

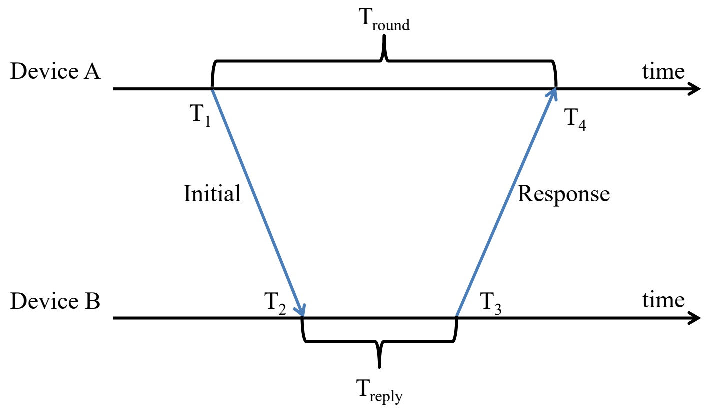

Figure 2.3: SS-TWR Scheme

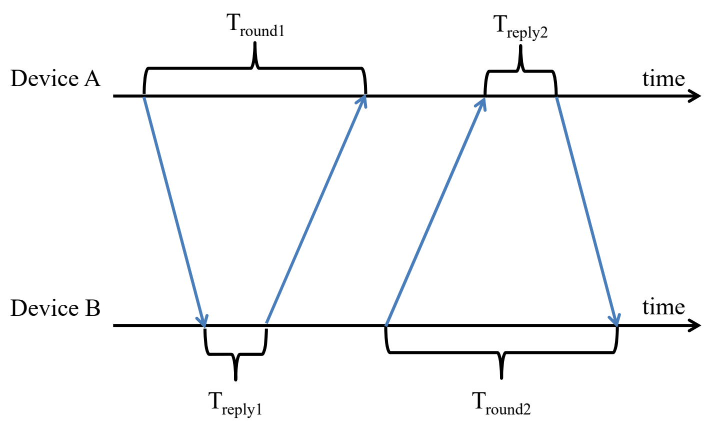

Figure 2.4: DS-TWR Scheme

The most common TWR schemes are single sided TWR (SS-TWR) and double sided TWR (DS-TWR), shown in Fig. 2.3 and Fig. 2.4, respectively.

SS-TWR utilizes one round message exchange between two nodes to obtain their distance. As Fig. 2.3 shows, device A sends an initial message to device B. The timestamps that device A sends out the message and device B receives the message are recorded locally, denoted by T_1 and T_2. After some delay time, denoted by T_{reply}, device B sends a reply message. In the message, it includes T_2 and T_3, the transmission time of the response message. Clearly, $T_3 = T_2 + T_{reply}$. Upon receiving the response message, device A records the receiving timestamp T_4. The propagation delay is then computed by (2.3). Because T_{round} and T_{reply} are both calculated locally, device A and device B need not be synchronized.

$$T_{PROP} = \frac{(T_4 - T_1) - (T_3 - T_2)}{2} = \frac{T_{round} - T_{reply}}{2} \tag{2.3}$$

When the clocks on the two devices have different skew, SS-TWR suffers from large estimation errors. DS-TWR, doubling the number of messages in SS-TWR (Fig. 2.4), is an extension of SS-TWR, which could drastically reduce the error compared to SS-TWR. We analyze sources of errors time-domain approaches in Section 4.1. The propagation delay is calculated by (2.4). When T_{reply1} is equal to T_{reply2}, it is also known as symmetric DS-TWR.

$$T_{PROP} = \frac{T_{round1} - T_{reply1} + T_{round2} - T_{reply2}}{4} \tag{2.4}$$

Note that in both TWR schemes, the two devices are symmetrical. In summary, the TWR technique has some advantages and disadvantages. The advantages are (1) targets perform ranging to reference nodes and compute its own location; and (2) there is no need to synchronize the devices. The primary disadvantages are that the method results in more energy consumption and longer location fix time as more message exchanges are required for localization. Lastly, TWR requires a wireless transceiver to be able to record accurate timestamps when messages are transmitted or received. This is not possible using software-based solutions.

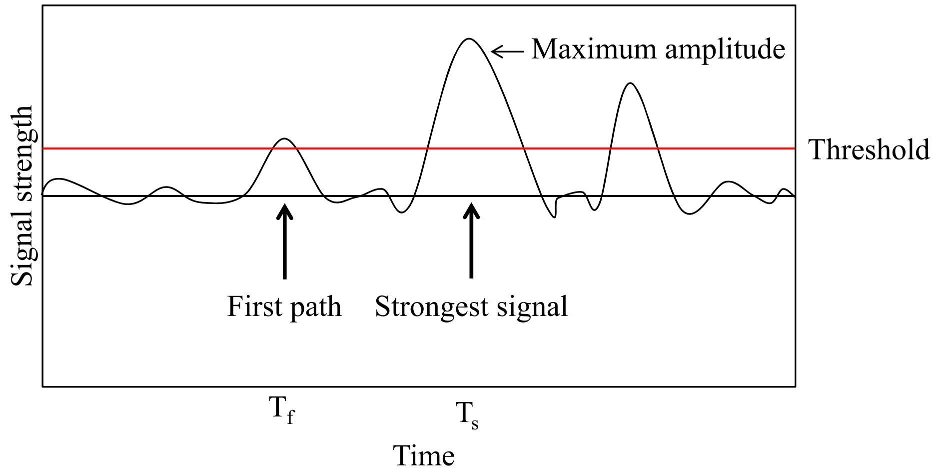

Figure 2.5: UWB CIR view for multipath scenario

2.4 Outlier Detection

Since a calculated location deviates from its ground truth location drastically when UWB signals propagate in multipath and NLOS scenarios, outlier detection is a pivotal function for precise positioning. If the channel impulse response (CIR) is available in the physical layer, multipath and NLOS scenarios can be distinguished from LOS ones. When such information is not available, surrogate metrics based on received signal strength (RSS) can be adopted including, RSSI, the maximum amplitude of the received signal, power difference and power ratio between estimated receiving signal level and estimated first path signal level. As illustrated in Fig. 2.5, the use of RSSI and the maximum amplitude of the received signal method is motivated by the fact that if the amplitude is below a certain threshold, it is more likely to be NLOS. The use of power difference and power ratio are motivated by the fact that a CIR with a high difference between the power of the received first path signal and the estimated receiving signal power according to the Friis transmission formula [42] is likely from a NLOS or multipath. Other metrics are based on either time delay

Table 2.3: Classification accuracy of different NLOS Metrics [3]

Metric	**LOS(%)**	**NLOS(%)**
Kurtosis	91.8	88.6
Skewness	78.2	98.7
Peak-to-lead delay	64.5	54.9
Power difference	63.4	57.2
Power ratio	54.8	60.7

(e.g., RMS delay-spread, peak-to-lead delay) or features of CIR (e.g., kurtosis and skewness) [43, 3, 44, 45]. RSS based metrics require little time to compute, and are supported by the DW1000 chip. In contrast, temporal and CIR features require seconds to produce a decision [3], which can degrade the performance of real-time localization system (RTLS). Silva et al. [3] showed the classification accuracy of those metrics in a NLOS scenario (Table. 2.3).

Chapter 3

Solution Approach

3.1 System Architecture

As shown in Fig. 3.1, the UWB-based IPS this thesis proposes is composed of three types of devices, also known as the local server, anchor nodes and tags. Both the TWR and TDOA approaches have been implemented on this platform. An anchor node is equipped with a UWB module, a WiFi module, a micro controller unit (MCU), and a pressure sensor. Anchor nodes are deployed at fixed known locations in the indoor environment. They are designed to collect all timestamps and information from tags and upload them to the server. A tag is equipped with a UWB module, a MCU, and a IMU sensor module to communicate with each anchor node one by one if TWR-based trilateration is applied, or to broadcast periodically if TDOA is used in localization. The purpose of the server is to obtain and log all the information from anchor nodes and compute tags' locations. For TWR-based solution, we implement a more efficient variant of DS-TWR called Three-Message DS-TWR (TMDS-TWR) and use power difference to detect outliers. A wireless synchronization solution is

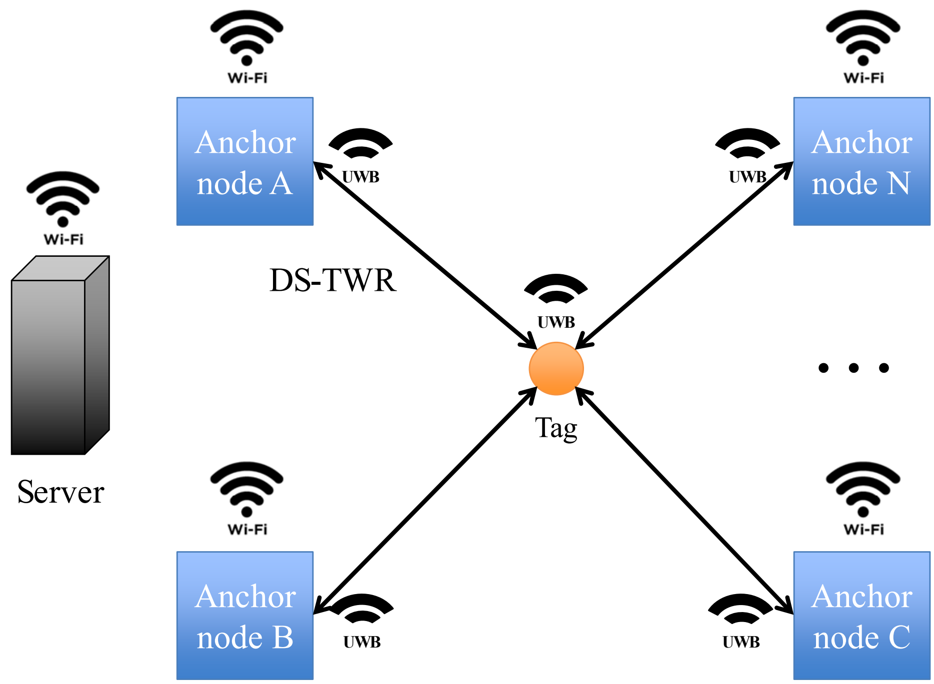

Figure 3.1: System architecture

developed for TDOA-based localization. In this case, one of the anchor nodes is set as a synchronization node, whose a local clock is used as the global time of the system. It broadcasts synchronization messages periodically, so that all the other anchor nodes in the vicinity align their local time with the global time.

3.2 Three-Message DS-TWR

Different from basic TWR schemes described in Section 2.3.3, Decawave [1] has proposed a more efficient DS-TWR method, named TMDS-TWR. TMDS-TWR is as accurate as DS-TWR, but has better efficiency and less energy consumption by sending one less message (Fig. 3.2).

An independently derived proof of this equation and error analysis can be found in

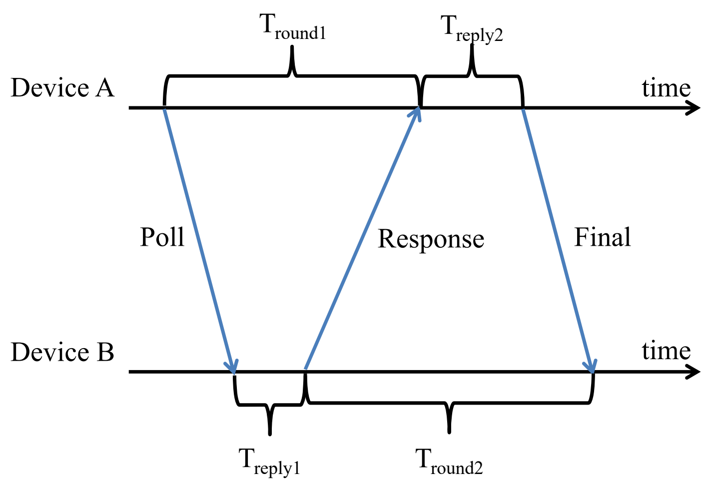

Figure 3.2: Three messages DS-TWR Scheme

Section 4.1. The three messages in TMDS-TWR are poll message, response message and final message. The detailed format for each message is provided in Section 5.2. In TMDS-TWR, a tag first sends out a poll message to initiate a single range measurement. Second, the anchor node sends back a response message to the tag after a time delay, denoted by T_{reply1}, upon reception of the poll message. The final message is sent by the tag after receiving the anchor's response message. Both the poll message and the response message could have empty payloads. However, the final message from the tag must include all the timestamps it has recorded: poll message sending timestamp, response message receiving timestamp and final message sending timestamp. After the anchor node has received the final message, it uploads all the received timestamps and those it recorded when receiving and sending messages during the TMDS-TWR round to the server. With these six timestamps, the distance between the tag and the anchor node is determined by (3.1).

$$T_{PROP} = \frac{T_{round1} \times T_{round2} - T_{reply1} \times T_{reply2}}{T_{round1} + T_{round2} + T_{reply1} + T_{reply2}}. \tag{3.1}$$

3.3 Wireless Synchronization for TDOA Estimation

As mentioned in Section 2.3, all the anchor nodes must be precisely synchronized to allow TDOA-based localization. The main challenge lies in how to synchronize all the anchor nodes precisely, because one nanosecond timing error generates $30cm$ of distance error. Recently published literatures on synchronization show various approaches, which fall into two broad categories: wired synchronization and wireless synchronization. In the case of wired synchronization, all the anchor nodes are connected to a central clock source through a wired network and use this clock as their system clock, or use it to periodically calibrate their local clock [46, 47]. The quality of the central clock and the delay introduced by the wires determine the performance of wired synchronization. This type of synchronization is easy to implement and can be quite accurate, but very costly compared to wireless synchronization in distributed environments. Wireless synchronization usually uses a synchronization node in a fixed and known position that broadcasts packets periodically to other anchors. Since the locations all anchor nodes and the synchronization node are known, the propagation times between the synchronization node and the anchors are known as well. As a result, all the anchors can be synchronized with the packet arrival times [48, 49, 50, 51]. In this work, we implement a wireless synchronization approach first proposed by Tiemann et al. [27].

The solution is shown in Fig. 3.3. Assuming there are two anchor nodes (AN#1 and AN#2), a tag and a synchronization node in the testbed. Let $\hat{t}_1^k$ and $\hat{t}_2^k$, $\hat{t}_1^{k+1}$ and $\hat{t}_2^{k+1}$be the reception local timestamps of the k^{th} and $k+1^{th}$ synchronization

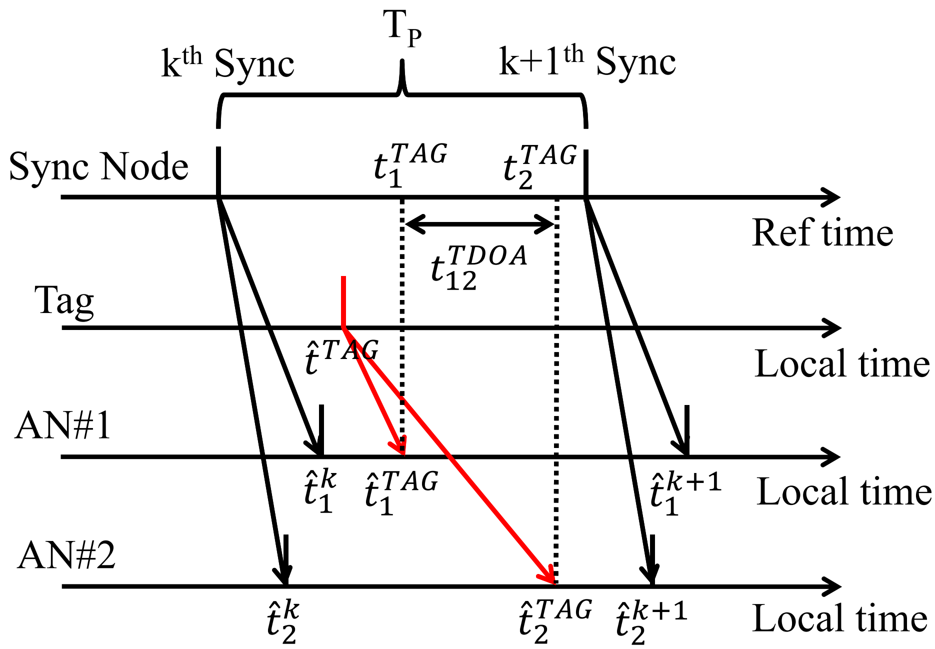

Figure 3.3: Illustration of wireless synchronization scheme

packets by the anchor nodes, respectively. Let T_P be the period of synchronization. Obviously, we can infer that

$$T_P = \hat{t}_1^{k+1} - \hat{t}_1^k = \hat{t}_2^{k+1} - \hat{t}_2^k. \tag{3.2}$$

If anchor nodes have received TDOA message from the tag at local time $\hat{t}_1^{TAG}$ and $\hat{t}_2^{TAG}$ respectively, $\hat{t}_1^{TAG}$ and $\hat{t}_2^{TAG}$ in the synchronizer's clock (denoted by t_i^{TAG}, $i = 1, 2$) can be represented by,

$$t_i^{TAG} = T_P \times (\frac{\hat{t}_i^{TAG} - \hat{t}_i^k}{\hat{t}_i^{k+1} - \hat{t}_i^k} - k), i = 1, 2. \tag{3.3}$$

As a result, the TDOA between AN#1 and AN#2 can be given by,

$$t_{12}^{TDOA} = t_1^{TAG} - t_2^{TAG} = T_P \times (\frac{\hat{t}_1^{TAG} - \hat{t}_1^k}{\hat{t}_1^{k+1} - \hat{t}_1^k} - \frac{\hat{t}_2^{TAG} - \hat{t}_2^k}{\hat{t}_2^{k+1} - \hat{t}_2^k}). \tag{3.4}$$

3.4 Outlier Detection

Outlier detection in the work is based on the power difference method mentioned in Section 2.4. This method has a lower classification accuracy (Table. 2.3), but its computation demand and processing time are much less than methods that use more complex CIR. Note that, DWM1000 UWB module offers built-in UWB signal diagnostic capability, and access to CIR.

Let P_D be the power difference defined as (3.5):

$$P_D = P_{ERP} - P_{EFP}, \tag{3.5}$$

where P_{ERP} represents the estimated receive power level (in dBm), and P_{EFP} represents the estimated first path power level (in dBm). They can be calculated using (3.6) and (3.7), respectively, provided by DW1000 user manual [1].

$$P_{ERP}\ dBm = 10 \times \log_{10}\left(\frac{C \times 2^{17}}{N^2}\right) - A, \tag{3.6}$$

and

$$P_{EFP}\ dBm = 10 \times \log_{10}\left(\frac{F_1^2 + F_2^2 + F_3^2}{N^2}\right) - A, \tag{3.7}$$

where C is the CIR power value, N is the preamble accumulation count value, A is the constant 121.74 for our setting, while F_1, F_2 and F_3 are the first path amplitude points

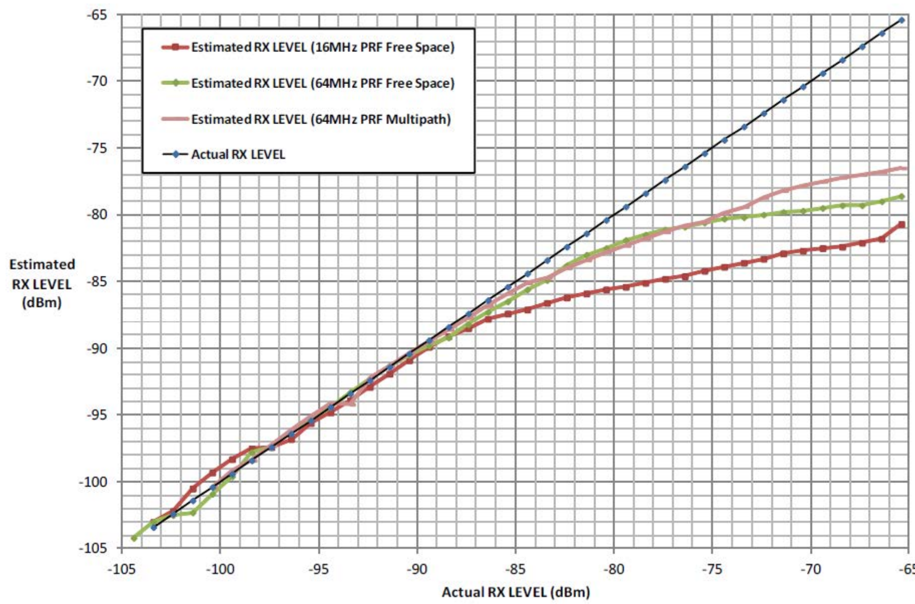

Figure 3.4: Estimated RX power versus actual RX power from Decawave user munal [1]

magnitude values. All those parameters are reported in the registers of DWM1000 UWB module after receiving a UWB packet [1].

The (3.6) is an estimation of the Friis transmission formula [42] given by Decawave. The user manual presented the relationship between the actual receive power and the power estimated by this technique(Fig. 3.4).

The (3.7) is the estimated first path received power level based on CIR recorded by DW1000 chipset. A proper threshold is needed to be set for P_D to identify the outliers to minimize the misclassification rate:

$$\begin{cases} If\ P_D > TH,\ Outlier, \\ If\ P_D \leq TH,\ Notoutlier. \end{cases} \tag{3.8}$$

We determined 12 as the absolute threshold setting for the system based on the experiments described in Section 6.1.1.

Chapter 4

Error Analysis

IPS is based on time-domain location approaches, all anchor nodes and tags must be equipped with hardware oscillators to record timestamps. However, all clocks are subject to drifts and offsets. Moreover, the oscillator frequency varies with physical conditions such as temperature and humidity, resulting in ranging errors.

Before analyzing the sources of error that exist in the time-domain location approaches, we first present basic concepts and assumptions. A local clock can be characterized by a linear equation [52],

$$T(t) = (1 + e) \times t + \mu = a \times t + \mu, \tag{4.1}$$

where $T(t)$ is the local time according to the oscillator, t is the global time or reference time, both e and a can be called the oscillator drift, and μ is the offset to global time. Usually, e is a few parts per million (ppm). A perfect clock's e and μ would be zero. If we compare the local times of two nodes, then, e and a are called relative drift, and μ is relative offset. If $e = 0$, and $\mu = 0$, it means the clocks have perfectly

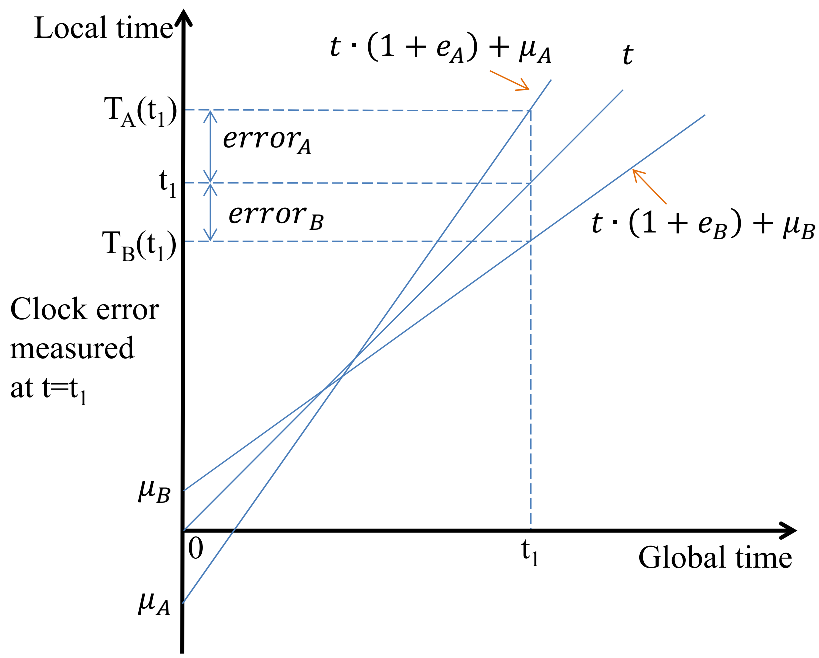

Figure 4.1: Illustration of the clock error due to clock drift and clock offset

synchronized. Typically, e and μ vary over time. Equivalently, one can introduce the notion of frequency drift and frequency offset.

A digital circuit system usually uses a time counter. With an oscillator frequency f, the counter increments automatically after $1/f$ second has elapsed. Therefore, the clock time can be represented by $t = \frac{n}{f}$, where n is the counter value. Fig. 4.1 gives an illustration of the clock error at t_1 due to clock drift and clock offset. In this chapter, all error analysis is based on the model represented by (4.1), and for convenience we assume e and μ are constants. In Section 4.1, we analyze the ranging error in TWR approaches from clock drifts and offsets. Another key error source is from the hardware delay, also known as antenna delay, which will be discussed in Section 4.2. Finally, we analyze errors in wireless synchronization.

4.1 Error Analysis of Two Way Ranging Schemes

Three different kinds of TWR approaches have been presented in Section 2.3.3 and Section 3.2. In this section, we analyze their performance.

Let e_A and e_B be the clock drift of device A and B; $\hat{T}_{PROP}$ and T_{PROP} are the estimated and true TOA. Therefore, the localization error can be represented by $error = \hat{T}_{PROP} - T_{PROP}$. Assume the clock offset of device A and device B be zero, because the offsets can be trimmed as long as antenna delay is calibrated.

For the SS-TWR approach,

$$\begin{aligned} \hat{T}_{PROP} &= \frac{T_{round} \times (1 + e_A) - T_{reply} \times (1 + e_B)}{2} \\ &= \frac{T_{round} - T_{reply}}{2} + \frac{T_{round} \times e_A - T_{reply} \times e_B}{2}. \end{aligned} \tag{4.2}$$

We then substitute (2.3) into (4.2),

$$\begin{aligned} \hat{T}_{PROP} = T_{PROP} &+ \frac{(2 \times T_{PROP} + T_{reply}) \times e_A - T_{reply} \times e_B}{2} \\ &= T_{PROP} + T_{PROP} \times e_A + \frac{T_{reply} \times (e_A - e_B)}{2}. \end{aligned} \tag{4.3}$$

Therefore, the SS-TWR clock error is given by

$$\begin{aligned} error &= \hat{T}_{PROP} - T_{PROP} \\ &= T_{PROP} \times e_A + \frac{T_{reply} \times (e_A - e_B)}{2}. \end{aligned} \tag{4.4}$$

Compared with T_{reply}, T_{PROP} is negligible, since T_{TOF} is on the order of 10^{-8} and T_{reply} is on the order of 10^{-5}. We have

$$error_{SS-TWR} \approx \frac{T_{reply} \times (e_A - e_B)}{2}. \tag{4.5}$$

In DS-TWR, we have

$$\hat{T}_{PROP} = T_{PROP} + T_{PROP} \times \frac{e_A + e_B}{2} + (T_{reply1} - T_{reply2}) \times \frac{(e_A - e_B)}{4}. \tag{4.6}$$

Thus, the DS-TWR clock error can be represented by

$$error_{DS-TWR} \approx (T_{reply1} - T_{reply2}) \times \frac{(e_A - e_B)}{4} \tag{4.7}$$

From 4.5 and 4.7, we see that the dominant error source is either T_{reply} or the difference of T_{reply1} and T_{reply2}. Although the difference of T_{reply1} and T_{reply2} can be made small by setting them close (Symmetrical DS-TWR), it is challenging to do so on two devices with different clocks. For TMDS-TWR, the equation to compute propagation time by Decawave is quite different from 4.4 and 4.6. From Barclay's thesis [53], we find that the key to the TMDS-TWR approach was to calculate the time of flight in a virtual clock, which is the mean value between the local clocks of device A and device B. That is, let a represent $(1 + e_A)$, and b represent $(1 + e_B)$. Then, the virtual clock is $\frac{a+b}{2} \times t$, where t is the global time. If $\frac{a+b}{2}$ is one, the virtual clock is perfectly synchronized with the global clock. Consequently, we can obtain the following equations from Fig. 3.2.

$$a \times T_{round1} = 2 \times T_{PROP} + b \times T_{reply1} \tag{4.8}$$

$$b \times T_{round2} = 2 \times T_{PROP} + a \times T_{reply2} \tag{4.9}$$

$$\frac{a+b}{2} = 1 \tag{4.10}$$

From (4.10), we get

$$b = 2 - a. \tag{4.11}$$

By substituting 4.11 into 4.8 and 4.9, we have:

$$a = \frac{2 \times (T_{reply1} + T_{PROP})}{T_{round1} + T_{reply1}} = \frac{2 \times (T_{round2} - T_{PROP})}{T_{round2} + T_{reply2}}. \tag{4.12}$$

This leads to 3.1. We can simply get the TMDS-TWR clock error equation:

$$\begin{aligned} error_{TMDS-TWR} &= \hat{T}_{PROP} - T_{PROP} \\ &= \frac{a \times T_{round1} \times b \times T_{round2} - b \times T_{reply1} \times a \times T_{reply2}}{a \times T_{round1} + b \times T_{round2} + a \times T_{reply1} + b \times T_{reply2}} \\ &- \frac{T_{round1} \times T_{round2} - T_{reply1} \times T_{reply2}}{T_{round1} + T_{round2} + T_{reply1} + T_{reply2}} \\ &= T_{PROP} \times (\frac{T_{round1} + T_{round2} + T_{reply1} + T_{reply2}}{\frac{T_{round1}+T_{reply2}}{1+e_b} + \frac{T_{round2}+T_{reply1}}{1+e_a}} - 1) \end{aligned} \tag{4.13}$$

Because e_a and e_b are constants on the order of 10^{-6} in (4.13), $\frac{T_{round1}+T_{reply2}}{1+e_b} + \frac{T_{round2}+T_{reply1}}{1+e_a}$ is approximately equal to $T_{round1} + T_{round2} + T_{reply1} + T_{reply2}$. Thus, we see that the dominant error source is T_{PROP}. Compared with (4.5) and (4.7), (4.13) explains the lower errors of TMDS-TWR.

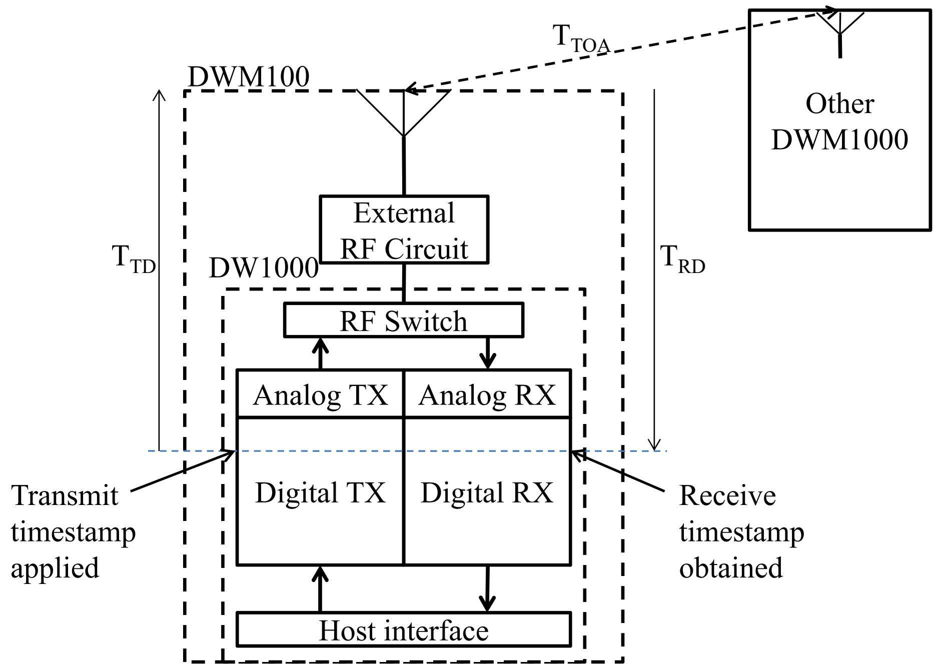

Figure 4.2: Illustration of antenna delay

4.2 Antenna Delay

The transmission and reception timestamps reported by DW1000 are not the actual timestamps due to delays caused by imperfection of chips, component varieties in the circuit, antenna and even environment effects, which are all device dependent. The measured $\hat{T}_{PROP}$ time can be presented by

$$\hat{T}_{PROP} = T_{TD} + T_{PROP} + T_{RD}, \quad (4.14)$$

where T_{TD} is the transmitting antenna delay, T_{RD} is the receive antenna delay, T_{PROP} is the true signal propagation time. Transmitting antenna delay and receive antenna delay are introduced by the hardware path for UWB signal transmitting and receiving (Fig. 4.2).

Although antenna delay is on the order of $10^{(-9)}$, such an error can significantly degrade distance estimation accuracy. For example, $1ns$ timing error translates to a $30cm$ distance error in term of the radio signal's flight time in the air.

The application note APS014 from Decawave proposed a TWR antenna delay calibration technique by which the antenna delay can be determined by minimizing the norm of the difference between the true distances matrix and the measurement distances matrix. Details are described in [54]. According to the application note, we can calibrate three PCB boards each time. First, we set their default antenna delay to zero. Then put two of them at known place, set one of them as tag and set the other one as anchor node, and record TWR distance measurements. After that, change the role of them, get the distance measurements again. In all, we can obtain a measurements matrix $EDM_{measured}$, which is,

$$EDM_{measured} = \begin{bmatrix} 0 & d_{12} & d_{13} \\ d_{21} & 0 & d_{23} \\ d_{31} & d_{32} & 0 \end{bmatrix}, \tag{4.15}$$

where d_{ij} is the mean of distance measurements from device i to device j when device i is set as tag. Then, the antenna delay can be determined by minimizing the norm of the difference between actual distance matrix EDM_{actual} and $EDM_{measured}$ [54].

$$min_{\forall\tau}||EDM_{actual} - EDM_{measured}||. \tag{4.16}$$

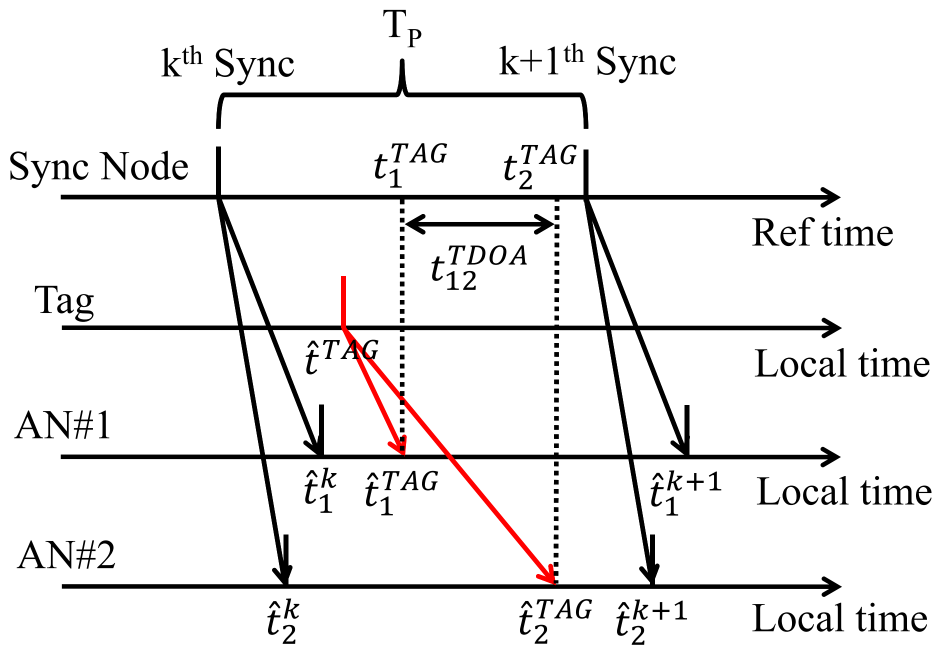

Figure 4.3: Illustration of wireless synchronization scheme

4.3 Errors in Wireless Synchronization

In Section 3.3, we introduced the wireless synchronization method implemented in our system. From (3.4), we know that, the measured time due to clock drift can be represented as

$$\hat{t}_{12}^{TDOA} = T_P \times (1 + e_{ref}) \times (\frac{\hat{t}_1^{TAG} - \hat{t}_1^k}{\hat{t}_1^{k+1} - \hat{t}_1^k} - \frac{\hat{t}_2^{TAG} - \hat{t}_2^k}{\hat{t}_2^{k+1} - \hat{t}_2^k}), \tag{4.17}$$

where e_{ref} is the clock drift of the reference node. Note that the clock drifts of AN#1 and AN#2 have been eliminated because the TDOA is only relevant to the proportion of the local timestamps. The clock error can be determined by subtracting (3.4) from (4.17)

$$
\begin{aligned}
error_{TDOA} &= e_{ref} \times T_p \times \left(\frac{\hat{t}_1^{TAG} - \hat{t}_1^k}{\hat{t}_1^{k+1} - \hat{t}_1^k} - \frac{\hat{t}_2^{TAG} - \hat{t}_2^k}{\hat{t}_2^{k+1} - \hat{t}_2^k}\right) \\
&= e_{ref} \times t_{12}^{TDOA}
\end{aligned}
\tag{4.18}
$$

From 4.18, the dominant error source of wireless synchronization TDOA solution is t_{12}^{TDOA}.

Chapter 5

Implementation

In this chapter, we first introduce the hardware design of anchor nodes and tags. Next, we discuss the UWB message formats. Finally, we present the firmware design and server design.

5.1 Hardware

For fast prototyping, we designed a single PCB board to use as both tag and anchor nodes (Fig. 5.1). The board can be configured as an anchor or a tag by changing the firmware and soldering different components. An anchor node contains a UWB module (DWM1000 [2]), WiFi module (ESP-WROOM-02 [6]), MCU (STM32F105 [5]), and a pressure sensor module (BMP280 [55]). We equipped tags with the same UWB module and MCU as anchor nodes. An IMU sensor module or other kinds of sensors can be added to the tag as well. In this work, we have only verified the circuit-level functions, but we have not integrated the IMU sensor and UWB ranging measurements. The MCU controls and communicates the DWM1000 and WiFi via high speed

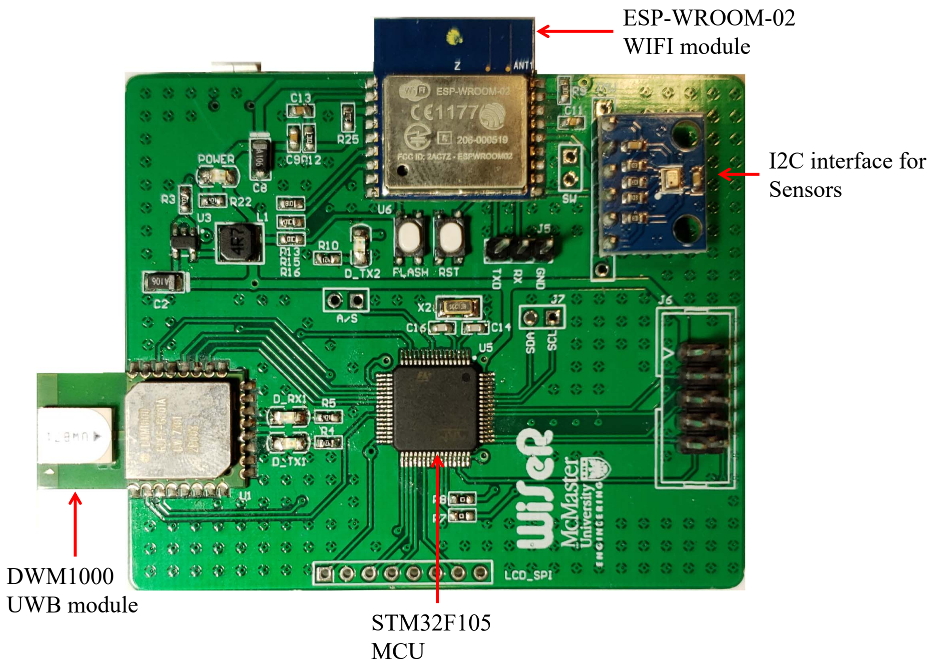

Figure 5.1: UWB-based IPS board

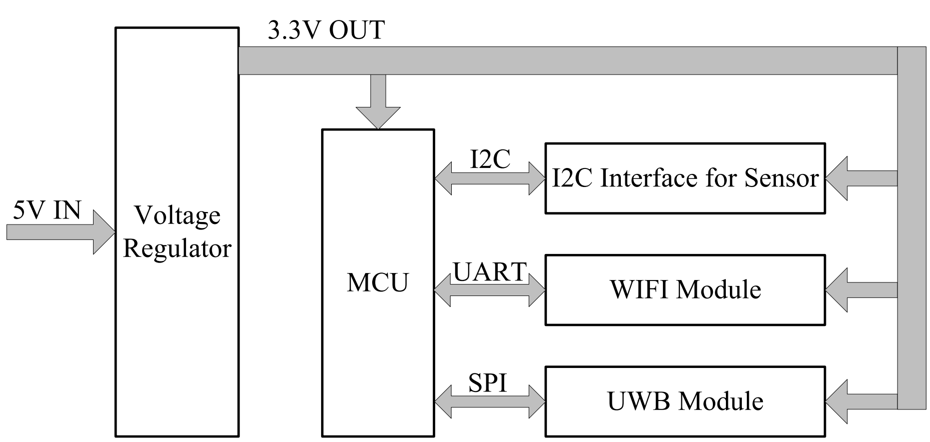

Figure 5.2: Anchor node and tag block diagram

SPI and UART. It obtains readings from external sensor via I2C. Fig 5.2 shows the block diagram of the UWB board.

5.1.1 Anchor Nodes and Tags

One of the core components for both anchors and tags is the DWM1000 UWB module manufactured by Decawave. The module consists of DW1000 UWB transceiver, an on board antenna, an oscillator and peripheral RF resistors and capacitors. DWM1000 enables cost effective (37.91 CAD per unit on Digikey.ca) and reduced complexity integration of UWB communications and ranging features. The DWM1000 module requires no RF design as antenna and associated analog and RF components are included in the module. The size of the module is only $13mm \times 23mm$. The DW1000 chip is a fully integrated low power, single chip CMOS radio transceiver IC that is compliant with the IEEE 802.15.4-2011 ultra-wideband (UWB) standard[56]. The main features are listed as follows [2]

- Achieve real time location of assets to an accuracy of $\pm 10cm$ using either TWR measurements or TDOA schemes.
- Span 6 RF bands from $3.5GHz$ to $6.5GHz$.
- Its high data rates allow it to keep on-air time short and cut down power consumption. Meanwhile, low data rates mean longer communication range (up to $200m$ with proper settings) and make it easier to find the first path timestamp.
- Provide access to CIR information from the received UWB signal waveforms. This process helps us to deal with severe multipath environments, making it

Table 5.1: IEEE 802.15.4-2011 UWB channels supported by DW1000 [1]

UWB Channel Number	**Center Frequency (MHz)**	**Band (MHz)**	**Bandwidth (MHz)**
1	3494.4	3244.8 - 3744	499.2
2	3993.6	3774 - 4243.2	499.2
3	4492.8	4243.2 - 4742.4	499.2
4	3993.6	3328 - 4659.2	1331.2
5	6489.6	6240 - 6739.2	499.2
7	6489.6	5980.3 - 6998.9	1081.6

Table 5.2: The electrical characteristics of ACS5200HFAUWB (2D) [4]

Frequency (MHz)		**3200**	**4200**	**5200**	**6200**
Gain (dB)	Peak	-0.88	2.73	2.51	4.16
	Average	-4.26	-1.22	-1.88	-1.10

suitable for NLOS rich conditions.

Table 5.1 shows the IEEE 802.15.4-2011 UWB channels supported by DW1000.

The on-board antenna's part number is ACS5200HFAUWB [4]. This particular antenna shows a uniform gain in the vertical field of the measured plane as shown in Fig. 5.3. Table. 5.2 summarizes the electrical characteristics of ACS5200HFAUWB.

The on-board $38.4MHz$ reference crystal has a drift range of $\pm$ $25ppm$. It was reported that further engineering work was done in production to reduce the initial frequency error to approximately $\pm$ 2 ppm under typical conditions [1]. However, we are not able to verify this experimentally.

In summary, Table 5.3 lists the characteristics of DWM1000.

Another essential component for both anchors and tags is the MCU. The MCU is used to execute ranging computation, read data from sensors, and control DWM1000 and the WiFi module. We select and implement STM32F105 in our board for its high computation speed and rich interfaces. An STM32F105 contains a high-performance

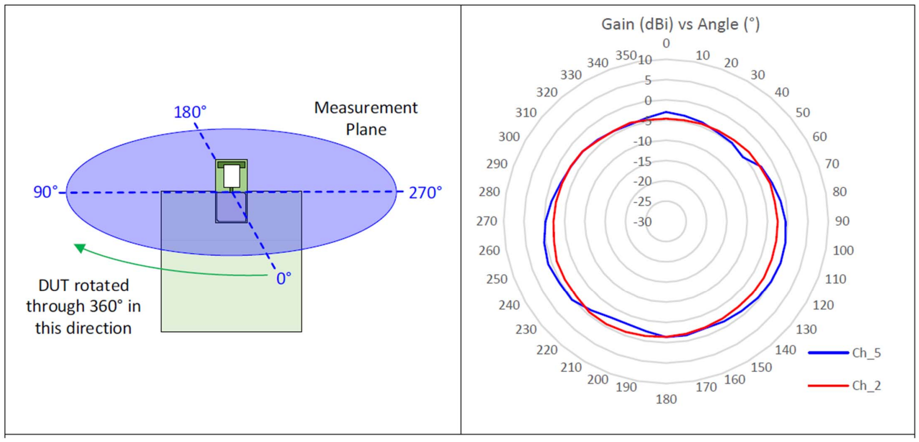

Figure 5.3: Measured Antenna Radiation Patterns in vertical plane[2]

Table 5.3: Characteristics of DWM1000 [2]

Parameter	**Min.**	**Typ.**	**Max.**	**Units**
Supply voltage	2.8	3.3	3.6	V
Supply current SLEEP mode		550		nA
Supply current IDLE mode		13.4		mA
Tx: 3.3 V supplies			140	mA
Rx: 3.3 V supplies			160	mA
Frequency range	3244		6999	MHz
Channel bandwidth		500		MHz
On-board crystal frequency		38.4		MHz
On-board crystal frequency stability with temperature			± 30	ppm
Output power spectral density (programmable)		-39	-35	dBm/MHz

Table 5.4: DC characteristics of STM32F105 [5]

Parameter	Min.	Typ.	Max.	Units
Supply voltage	2.4	3.3	3.6	V
Supply current SLEEP mode (8MHz)		3.2	3.7	mA
Supply current Run mode (72MHz)		47.3	65.5	mA

ARM Cortex -M3 32-bit RISC core operating at a 72 MHz frequency, with high speed embedded memories (256 KB flash memory and 64 KB SRAM). There are two 12-bit ADCs, four general-purpose 16-bit timers, as well as standard and advanced communication interfaces. These interfaces include I2C, High speed SPI, USART and CAN [5]. The adoption of STM32F105 in fact has more computation power than needed in the UWB IPS system. This is by design as in the future, we plan to perform all computation on tags or anchor nodes instead of using a local server. In addition, we will fuse other sensor modalities with UWB, such as IMU readings. Table 5.4 lists the direct current (DC) characteristics of STM32F105.

Each anchor node has a WiFi module on board that communicates with its MCU via UART and uploads ranging information to the local server. We chose ESP-WROOM-02 in our design. The module size is 18 mm by 20 mm. The gain of the on-board PCB antenna is 2 dBi. The module integrates an enhanced version of Tensilica's L106 Diamond series 32-bit processor and on-chip SRAM. It can interface with external sensors and other devices through the GPIOs [6]. A Software Development Kit (SDK) provides sample codes for various applications. Since ESP-WROOM-02 works like an information transfer station, it can be other wireless communication techniques than WiFi if IPS requirements could meet. The reason we chose to use a

Table 5.5: DC characteristics of EPS-WROOM-02 [6]

Parameter	**Min.**	**Typ.**	**Max.**	**Units**
Supply voltage	2.7	3.3	3.6	V
Supply current SLEEP mode		0.9		nA
Supply current IDLE mode		15		mA
Tx: 3.3 V supplies		170		mA
Rx: 3.3 V supplies		56		mA

WiFi module for uploading timestamp information is that the UWB IPS we developed is required to be able to cover the Microsoft Indoor Localization Competition site described in Section 6.2 which is of size $15m \times 15m \times 10m$, a two floors historical building. Table 5.5 lists the DC characteristics of EPS-WROOM-02.

We incorporated a pressure sensor on both anchor nodes and tags initially to determine the height of tags and thereby improve 3D positioning accuracy. With pressure sensor measurements at different heights from the anchor nodes, the height of tags can be inferred since in indoor environments, pressure typically decreases linearly with increasing height. However, experiment results showed the pressure readings on the anchors varied over time due to the uncontrollable heat generated by DWM1000 and ESP-WROOM-02. We changed the design to include an IMU sensor instead.

From the DC characteristics of each component on anchor nodes and tags, we infer it can be estimated that the current usages for anchor nodes and tags are hundreds of mA at $3.3V$ when exchanging information via a UWB transceiver or WiFi. Our measurement study finds that power consumption of anchor nodes and tags in the TWR measuring mode are $720mW$ and $450mW$, respectively. Because the power source is from a MicroUSB port and all on-board components require a $3.3V$ voltage supply, we selected PAM2305AAB330 [57], an ultra high efficiency step-down DC/DC converter, to build the power regulator circuit. PAM2305AAB330 supports a range of input voltages from $3.6V$ to $5.5V$ with an output voltage at $3.3V$. The output current is up to $1A$ and the efficiency is up to 96%. Due to the power consumption of the board we developed, the board temperature rises dramatically during localization, which degrades the system performance. The trade-off between location updating and heat is difficult to balance.

5.1.2 Local Server

Currently, we use a laptop as the local server. The implementation is in python that aggregates the timestamps and estimates real time tag locations. In the future, we will consider moving the implementation to anchors and tags.

5.2 Message Format

In this thesis, we extend the message format proposed by Decawave by optimizing the length of messages to reduce transmitting time and accelerate TMDS-TWR speed. In subsequent sections, we first describe the IEEE 802.15.4 UWB physical layer and then introduce the general ranging frame format and message formats for TMDS-TWR in Decawave's implementation. Finally, we present a comparison between the proposed messages format and Dacawave's own format.

5.2.1 The IEEE 802.15.4 UWB Physical Layer

A synchronization Header (SHR) consists of the preamble sequence and the start of frame delimiter (SFD). In contrast to the BPM/BPSK modulation used for the

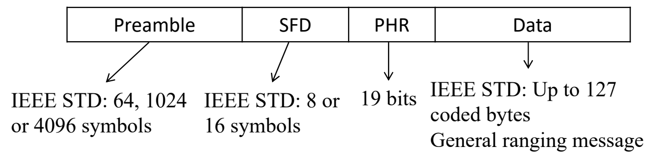

Figure 5.4: UWB PHY frame structure[1]

2 Bytes	1 Byte	2 Bytes		8 Bytes	8 Bytes	N Bytes	2 Bytes
Frame Control	Sequence Number	PAN ID		Destination Address	Source Address	Payload	FCS
		0xCA	0xDE				

Figure 5.5: General Ranging Frame Format[1]

PHR and data, a SHR is made up of pulses (called symbols). The average pulse repetition frequency (PRF) determines the pulses' duration and how many chips a symbol would be divided into. The DW1000 supports an average PRF of $16MHz$ and $64MHz$, corresponding to 496 chips and 508 chips per symbol, respectively. In the UWB PHY, the chirp frequency is $499.2MHz$, and thus the symbol times are $993.59ns$ for $16MHz$ PRF and $1017.63ns$ for $64MHz$ PRF[1]. With a known data rate, the time duration of PHR and data can be computed directly.

5.2.2 General Ranging Frame Format

There are a total of five messages employed in Decawave TWR example codes: two in the discovery phase (the blink message and the ranging initial message) and three in the ranging phase (the poll message, the response message, and the final message).

1 Byte	1 Byte	8 Bytes	2 Bytes
Frame Control	Sequence Number	Tag Address	FCS
0xC5			

Figure 5.6: Blink message Frame Format[1]

Table 5.6: UWB operation configuration

UWB Channel Number	**Center Frequency (MHz)**	**Data Rate (MHz)**	**PRF (MHz)**	**Preamble**
2	3993.6	110 kbps	64	1024

Although these messages follow IEEE message conventions, they are not standard RTLS messages. The general message format is specified by the IEEE 802.15.4 standard is given in Fig. 5.5. In the figure, the two bytes Frame Control (FC) octets vary among the messages - some use 8 byte (64 bit) addresses and others 2 byte (16 bit) addresses. A single 16-bit PAN ID is included in all messages with the exception of the blink message in TDOA approaches. Blink messages follow the format defined in the IEEE STD 802.15.4e-2012 (Fig. 5.6). The sequence number octet is incremented modulo-256 for every frame sent. The source and destination addresses are either 64-bit numbers programmed uniquely into each device (during production) or 16-bit addresses temporarily assigned. The 2-byte FCS is a CRC frame check sequence following the IEEE standard[1]. One can generate this automatically by the DW1000 IC and append it to the transmitted message.

The content in the payload portion of the frame, also referred to as application level payload, defines the type of ranging messages. Because the ranging initial message is not implemented in our system, we only introduce the poll message, the response message, and the final message payload formats next.

5.2.3 Poll, Response, and Final Message Frame Format

A tag sends a poll message to initiate a single range measurement. For the poll message, the payload portion of the frame is a single byte of the value 0x61 (Fig. 5.7a).

1 Byte
Function Code
0x61

(a) Poll message

1 Byte	4 Bytes
Function Code	Old TOA
0x50	

(b) Response message

1 Byte	5 Bytes	5 Bytes	5 Bytes
Function Code	Poll TX time	Response RX time	Final TX time
0x69			

(c) Final message

Figure 5.7: Ranging message encodings

An anchor sends the a response message in reply to a poll message from the tag. The response message is 5 bytes in length (Fig. 5.7b) and contains the TWR result from the last turn.

The tag sends the final message after receiving the anchor's response message. The final message is 16 bytes in length(Fig. 5.7c).

In the work, we optimize the messages format to accelerate TWR measurement.

Table 5.7: Messages format and messages encoding comparison

Message		**Decawave**	**In the work**
Message length	Blink/SYNC	12 bytes	15 bytes
	Poll	24 bytes	16 bytes
	Response	28 bytes	16 bytes
	Final	39 bytes	31 bytes
Transmitting time	Blink/SYNC	2001.9 μs	2198.82 μs
	Poll	2789.58 μs	2264.46 μs
	Response	3052.15 μs	2264.46 μs
	Final	3774.2 μs	3249.07 μs

We follow the Decawave message formats, but adjust the length of each message. Our UWB IPS requires the range distance to be as large as possible. From application note APS017 [58], there are five ways to improve ranging distance: operating in a lower channel, adopting longer preambles, a lower data rate and a larger PRF. Clearly, there is a trade-off between high update rates and large ranging distance. We select the UWB operation configuration in Table 5.6 to strike a good balance between the two.

Table 5.7 summarizes the length and transmission time of different messages in the Decawave reference design and in our system.

5.3 Firmware Design

In this section, we introduce the firmware for the MCU and WiFi modules adopted. The WiFi module obtains ranging timestamps and CIR information from the MCU and upload them to the local server. The implementation is based on UART API and WiFi API. We next present more details on the MCU firmware implementation.

Decawave has provided a comprehensive examples and application programming interfaces (APIs) to developers. We have optimized the TWR reference implementation to fulfill our requirements, and implemented TDOA algorithm using the those APIs.

Fig. 5.8a and Fig. 5.8b show the flow charts of the anchor node and tag operations for TMSD-TWR.

In TDOA, both tags and the synchronization node only need to transmit blink messages (Fig. 5.6) and synchronization messages periodically. The synchronization message is similar to a blink message with the exception of a 4-byte sequence number.

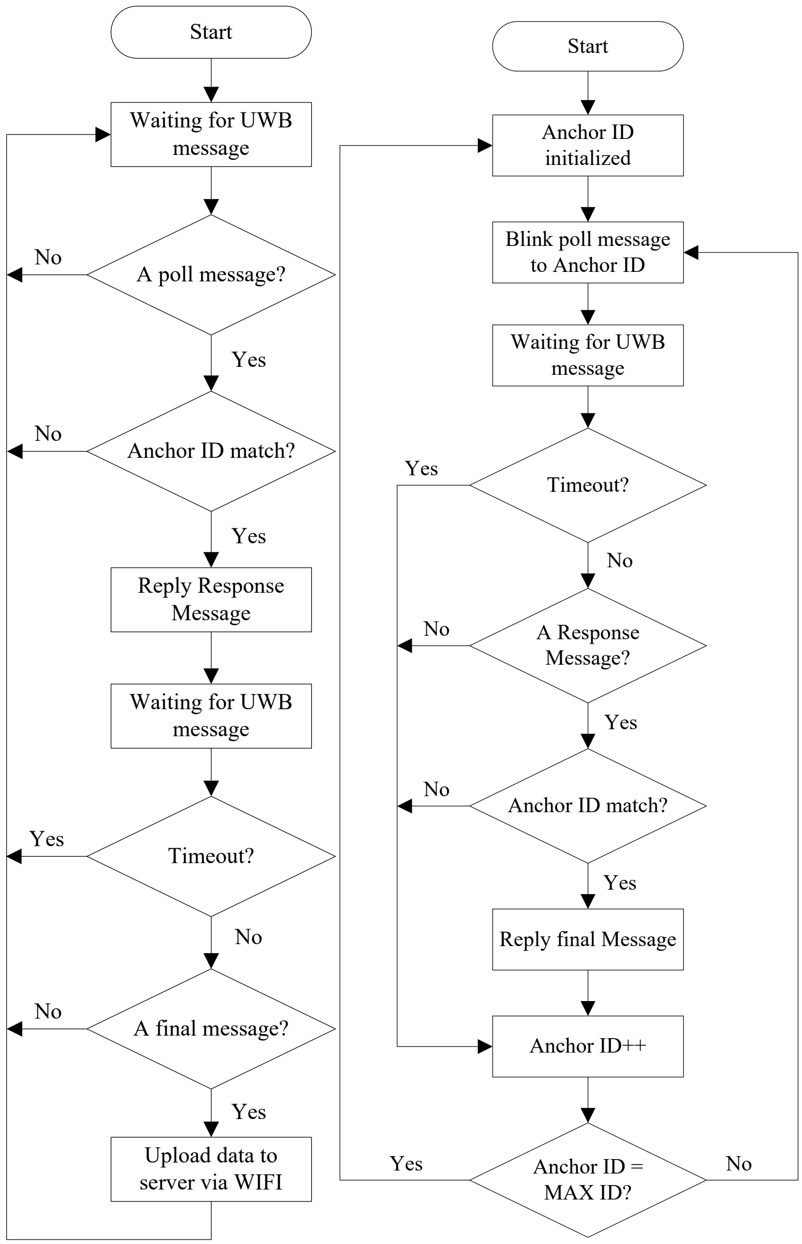

(a) Anchor Node (b) Tag

Figure 5.8: The TMDS-TWR approach firmware flow chart

The periods of blink and synchronization messages are configurable. In this thesis, the period of blink message is $7ms$ and the period of synchronization message is $53ms$.

Consequently, seven location estimates can be done between two synchronization messages.

5.4 Server Design

Server is used to collect all the information from anchor nodes and calculate the final locations. For both TMDS-TWR and TDOA, we adopt the least square method for locations estimation implemented by another student in our group [16].

Chapter 6

Evaluation

In this chapter, we first evaluate the performance of distance measurements based on TMDS-TWR and NLOS detection. We then present the performance of the TDOA approach in a lab environment. Finally, we evaluate indoor localization based on the TMDS-TWR approach in two experimental testbeds. All ground truth locations except for the ones in the second testbed are measured by a Leica DISTO S910 [59] laser distance measurer that captures multiple, accurate measurements in three dimensions from a single location. It achieves an accuracy of $\pm\ 2mm$ for point to point measurement with a range up to $300m$. It also outputs 3D coordinates of the target, which significantly improves the efficiency of common measuring tasks.

6.1 Evaluation of TMDS-TWR Distance Measurements and Outlier Detection

In this section, we first provide TMDS-TWR distance measurement results. By comparing the ranging errors with and without NLOS detection, we verify the effects of outlier detection and determine the threshold in different obstruction conditions. Before testing, we calibrate the antenna delay of each UWB board by the method presented in Section 4.2.

6.1.1 LOS Measurements

Figure 6.1: TWR evaluation in a hallway in McMaster university

We perform measurement tests in LOS conditions in a hallway in the information technology building located in the McMaster University campus (Fig. 6.1). In the experiments, we place an anchor node at a fixed location and vary a tag's distance

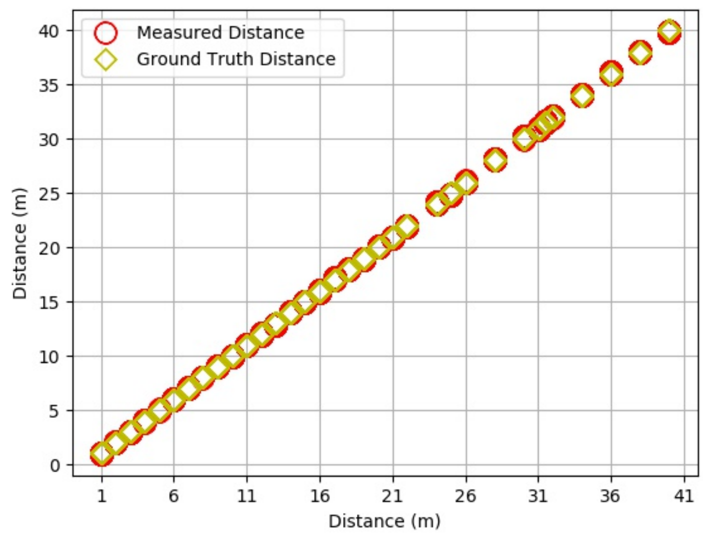

Figure 6.2: Comparison of measured distance and ground truth

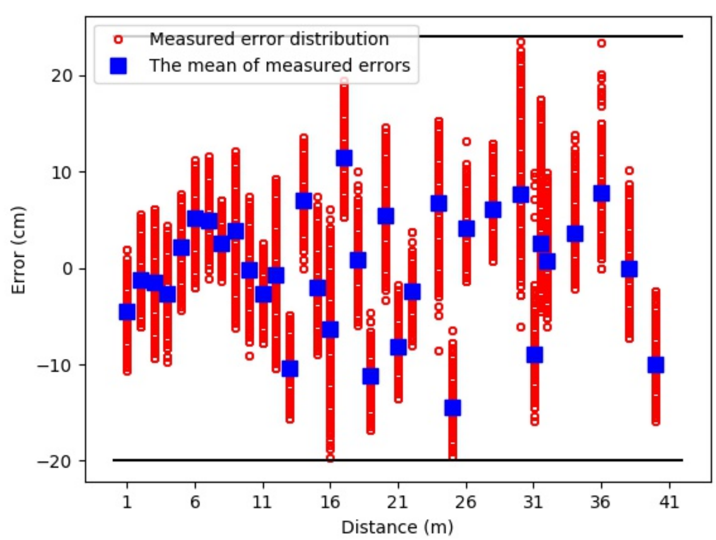

Figure 6.3: The distribution of measured errors and the mean of errors

Table 6.1: Five different anchor nodes 95%-quantile errors at five different positions

95%-quantile error (cm)	**Distance (m)**				
	8	13	16	19	22
Anchor#1	2.8	11.6	10.4	13.4	16.7
Anchor#2	4.6	11.5	12.8	11.0	16.7
Anchor#3	3.7	10.2	12.3	8.7	16.7
Anchor#4	3.2	10.6	11.4	12.0	17.1
Anchor#5	3.2	7.4	10.9	10.6	14.3

to the anchor from 1m to 40m along the hallway at a total of 34 known locations. Fig. 6.2 shows the ranging results. The errors at each reference point and their mean are shown in Fig. 6.3. We find that with outlier detection, the absolute mean ranging error is less than $15cm$, while the overall ranging error is less than $\pm 24cm$.

Table 6.1 lists ranging error with 95%-quantile errors at 5 different positions with 5 different anchors. We observe that the ranging performance is consistent across anchors.

6.1.2 Evaluation of Outiler Detection

Although the hallway is straight, outliers still exist due to the multipath. Fig. 6.4 shows the raw ranging errors and RSSI power difference before outlier removal. With the abnormal RSSI power difference readings, we observe that the outliers exist at the distance of $19m$ and $40m$. Compared to Fig. 6.3, which shows the errors after outlier removal by setting the power difference threshold to 12, we show that outlier removal improves the ranging accuracy.

To understand better the effect of blockages, we conducted another experiment and deployed two anchor nodes at $7m$ apart. Different obstructions are placed in front of one anchor node, including a door and a person. Fig. 6.5 shows the CDF of ranging

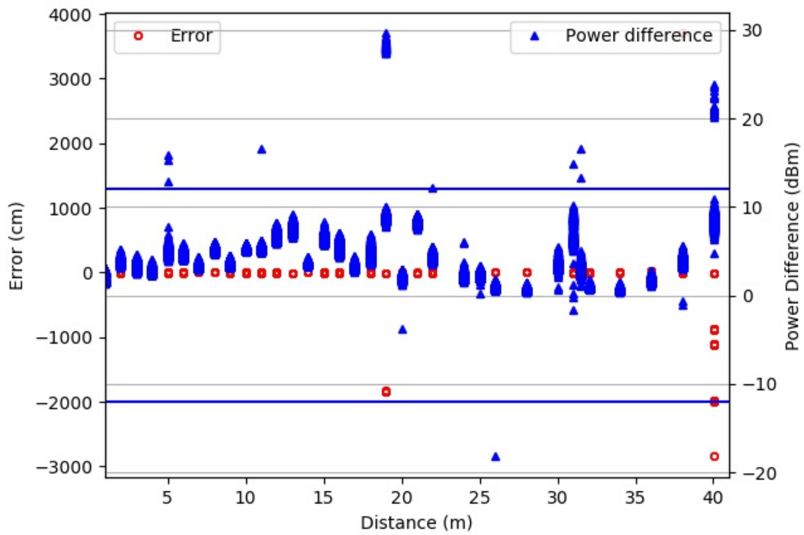

Figure 6.4: The comparison of raw measurement error and power difference distribution

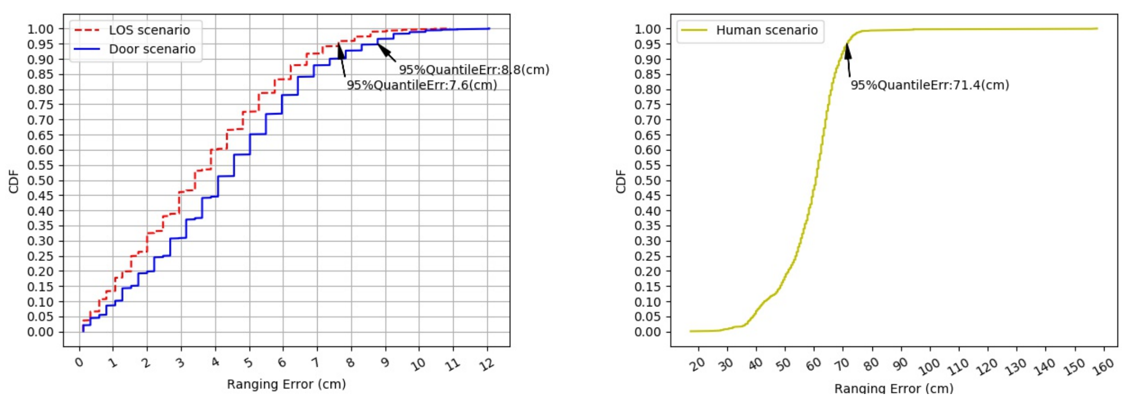

(a) LOS and door scenario (b) Human scenario

Figure 6.5: The comparison of CDF of localization errors in different scenarios

errors in the three scenarios. We observe that the ranging errors in human scenarios is much worse than those in LOS scenario and in door scenario. By comparing their power differences and ranging errors shown in Fig. 6.5 and Fig. 6.6, we can make two

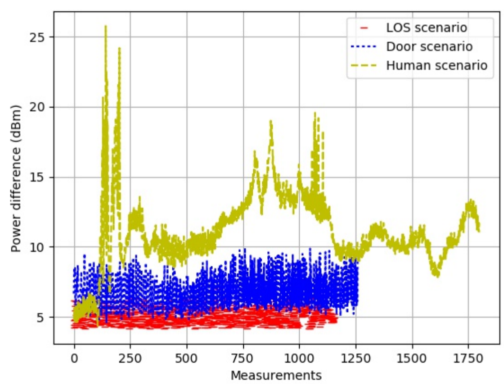

(a) The comparison of power differences in different scenarios

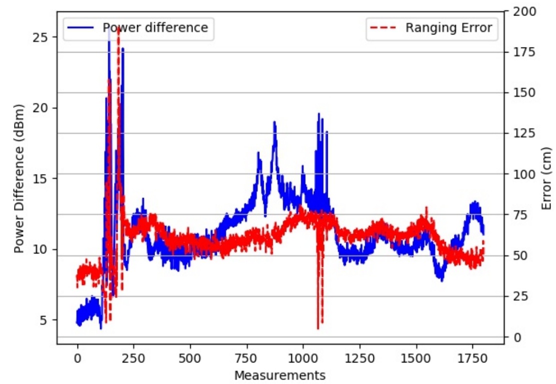

(b) The power difference and ranging error in Human scenario

Figure 6.6: The power differences in different scenarios

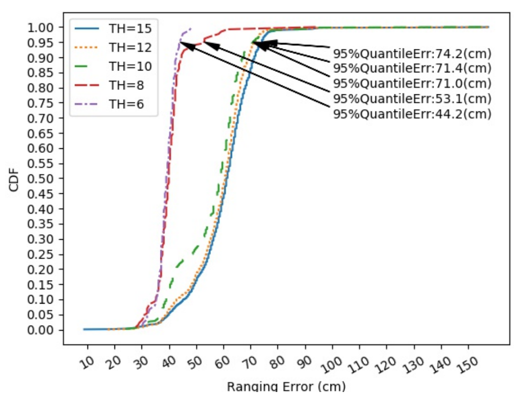

(a) The CDF of ranging errors with different power difference threshold setting in human scenario

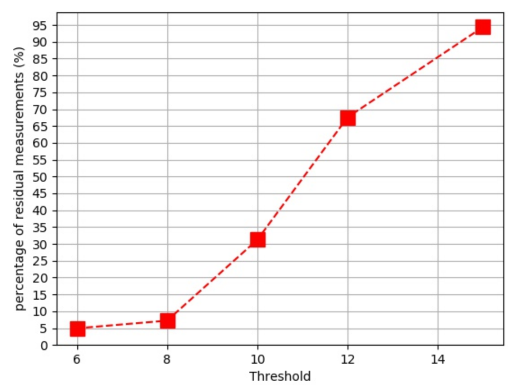

(b) The residual number of measurements with difference threshold setting in human scenario

Figure 6.7: The ranging performance with different power difference thresholds setting in human scenario

observations, 1) when there exists an obstruction, the RSSI power difference varies drastically; and 2) resulting measurement errors increase if RSSI power differences rise above a specific threshold. In Fig. 6.7, we investigate the effect of the threshold value in outlier removal. Clearly, as the threshold decreases, the ranging accuracy improves. However, there is a trade-off between threshold and location updating rate. In fact, with a small threshold, many measurements may be classified as NLOS conditions and would be removed (Fig. 6.7b). It is therefore essential to find a proper outlier threshold. We currently set it as 12 based the above evaluation results.

6.2 Testbed Setup

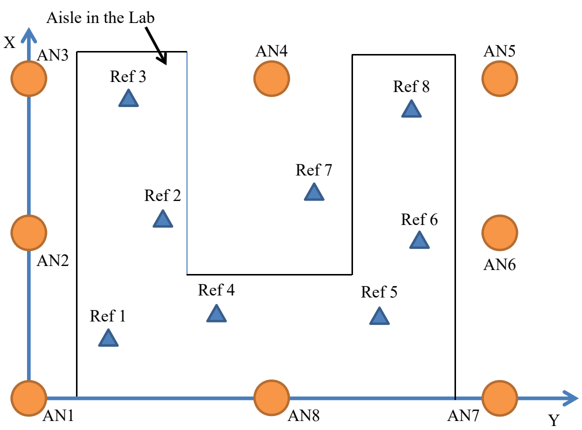

(a) The floor plan of the first testbed

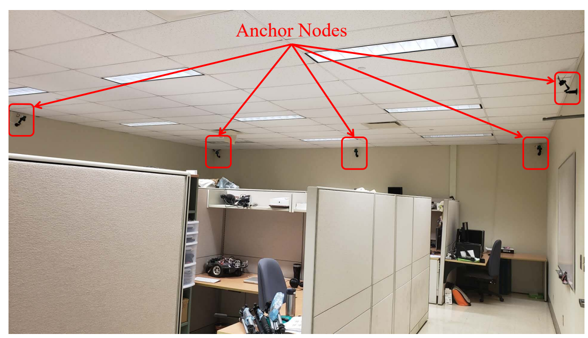

(b) A picture of the office environment and anchor nodes deployment

Figure 6.8: The first testbed: a general crowded office environment of size about $10.4m \times 7.4m$

There are two experimental testbed setups for evaluating TDOA based localization and TMDS-TWR based localization. In the first testbed, we permanently installed eight anchors on the wall near the ceiling of a $10.4m \times 7.4m$ office space. Fig 6.8 shows the floor plan of the testbed, the office environment and anchor nodes deployment. And Table. 6.2 gives the coordinates of anchor nodes and reference points. Because all the anchor nodes are deployed at similar heights due to space limits, the errors on z axis can be very large. We present 2D and 3D localization performances in the first

Figure 6.9: The second testbed: a larger and multipath rich environment of size about 15 m × 15 m × 10 m

testbed with different heights.

Table 6.2: Anchor nodes and reference points coordinates in the first testbed

Anchor Nodes	**Coordinate**			**Reference points**	**Coordinate**		
	X (m)	Y (m)	Z (m)		X (m)	Y (m)	Z (m)
AN#1	0.000	0.000	2.844	Ref#1	1.280	2.583	1.84/2.474
AN#2	3.606	0.000	2.859	Ref#2	4.619	3.180	1.84/2.475
AN#3	7.393	0.012	2.864	Ref#3	6.465	2.855	1.84/2.480
AN#4	7.473	5.273	2.861	Ref#4	0.979	4.405	1.84/2.471
AN#5	7.472	10.383	2.852	Ref#5	0.931	7.777	1.84/2.468
AN#6	3.613	10.399	2.852	Ref#6	2.722	8.058	1.84/2.463
AN#7	0.018	10.411	2.854	Ref#7	4.294	6.264	1.84/2.476
AN#8	-0.007	5.404	2.852	Ref#8	6.426	8.117	1.84/2.470

The second testbed is of size 15m × 15m × 10m (two floors) in the Bolsa Palace in Porto, Portugal, which was the 2018 Microsoft Indoor Localization competition site during the IPSN'18 conference. As part of the requirements, only 10 anchor nodes are permitted to be deployed in the area and participants are asked to provide real time locations while a person carrying the tag walks up the stairways and along the corridors. As shown in Fig. 6.9, the evaluation area can be divided into three parts: the first floor, stairs and the second floor. The first floor and second floor are separately by stone floors. There are large stone pillars in the areas. It is really a challenging space for IPS due to multipath propagation and various obstructions. During the evaluation, people were allowed to freely move around.

6.3 TDOA Indoor Positioning Performance

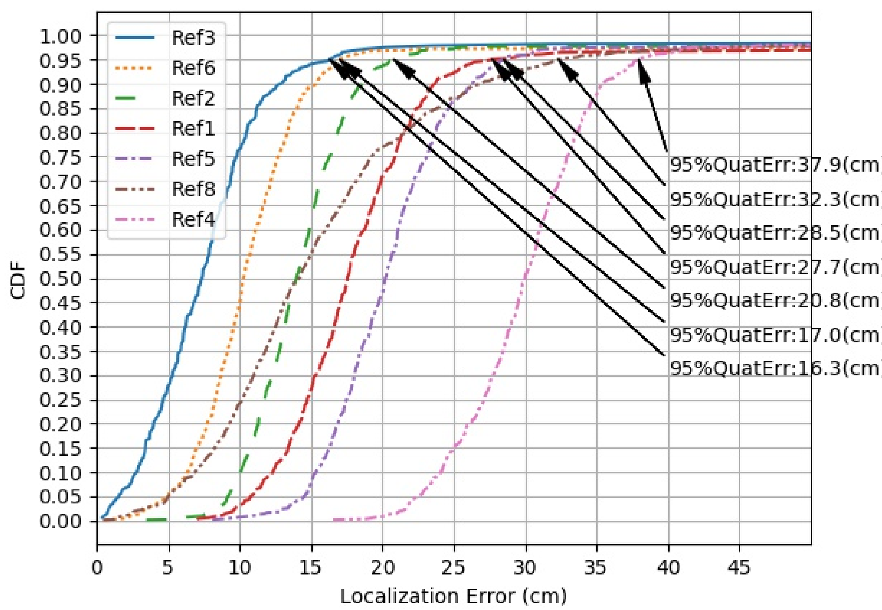

Figure 6.10: The CDF of 2D localization error at 7 reference points in the first testbed with TDOA approach

We have conducted a stationary positioning performance test in the lab to verify the 2D localization function and the accuracy of the TDOA approach. The test platform consists of eight anchor nodes, one tag and one synchronization node (placed at Ref#7) in the first testbed. The tag has been put at seven reference points with a fixed height. At least 600 fixes are collected at each points. Fig. 6.10 gives the CDF of the 2D location errors, which shows the 95%-quantile 2D localization errors are 27.7cm, 20.8cm, 16.3cm, 37.9cm, 28.5cm, 17.0cm, 32.3cm. As will become clear in Section 6.4, the accuracy achieved by TDOA-based location is worse than that from TMDS-TWR.

6.4 TMDS-TWR Indoor Positioning Performance

Fig. 6.11 presents the 2D and 3D stationary positioning performance at 8 reference points in the first testbed at different heights. At each reference point, at least 800 location fixes are collected. The 95%-quantile 2D and 3D localization errors can be found in Fig. 6.11. Comparing Fig. 6.11a with Fig. 6.11c, we can observe that the 2D localization errors are similar at different tag's heights. However, as evident in Fig. 6.11b with Fig. 6.11d, the 3D 95%-quantile localization errors vary a lot, which means that the estimated Z axis coordinates are far from the ground truth. This is due to the fact that all the anchor nodes are deployed at similar heights, resulting in a narrow measurement cubic. Thus, the errors on Z axis can be very large. In addition, during these tests, we find that the facing direction of the tag's antenna would affect performance. The best direction corresponds to orienting the tag's antenna towards the farthest anchor node which increases the signal-noise ratio (SNR) of the signals from the furthest anchor.

Also, we demonstrate how the number of anchor nodes would affect the localization accuracy. Fig. 6.12a presents the overall 95%-quantile 2D localization errors

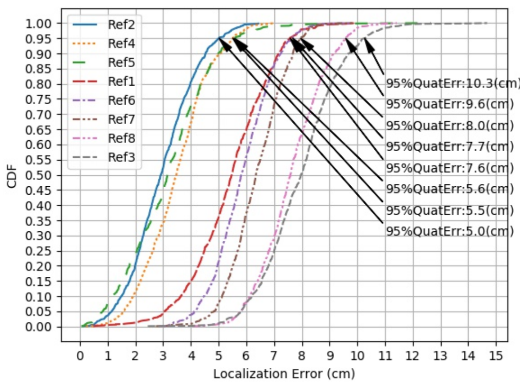

(a) The CDF of 2D stationary localization error at 1.84m height

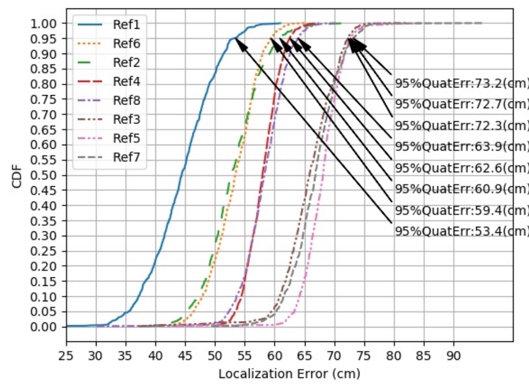

(b) The CDF of 3D stationary localization error at 1.84m height

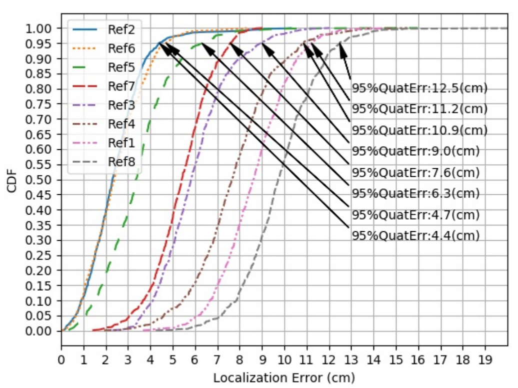

(c) The CDF of 2D stationary localization error at 2.4m height

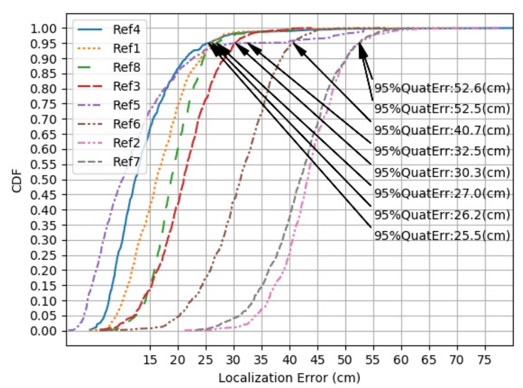

(d) The CDF of 3D stationary localization error at 2.4m height

Figure 6.11: The CDF of 2D and 3D stationary localization error at 8 reference points in the first testbed at different heights

for different number of anchor nodes used in the first testbed at 2.4m height. And Fig. 6.12b presents the relationship between 95%-quantile error and number of anchor nodes. The anchor nodes information can be found in Table 6.3. The result shows that the localization errors decrease while the number of anchor nodes used in the testbed increases.

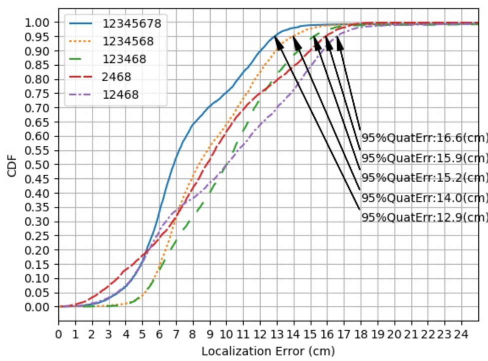

(a) The CDF of overall 2D static localization error for different number of anchor nodes at 2.4m heigh

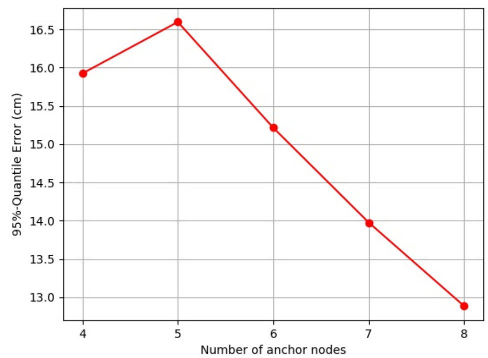

(b) The relationship between 95%-quantile error and number of anchor nodes

Figure 6.12: Localization errors for different number of anchor nodes used in the first testbed

Table 6.3: Anchor nodes information

Number of Anchor nodes	**AN#**
4	2, 4, 6, 8
5	1, 2, 4, 6, 8
6	1, 2, 3, 4, 6, 8
7	1, 2, 3, 4, 5, 6, 8
8	1, 2, 3, 4, 5, 6, 7, 8

Fig. 6.13a shows the scatter plot of localization results when the tag moves at $1m/s$ along the zigzag trajectory. Since we do not have the ground truth locations during the movements, the localization errors are estimated as the distance to the closest location on the trajectory. The 95%-quantile 2D localization errors in the zigzag trajectories is $28.9cm$ (Fig. 6.13b). The results are far from those in stationary localization experiments. This is due to the fact that we can not let the tag follow the zigzag trajectory perfectly. Since we held the tripod and walked through all the reference points, the swing of the tag and routing deviation are inevitable. In

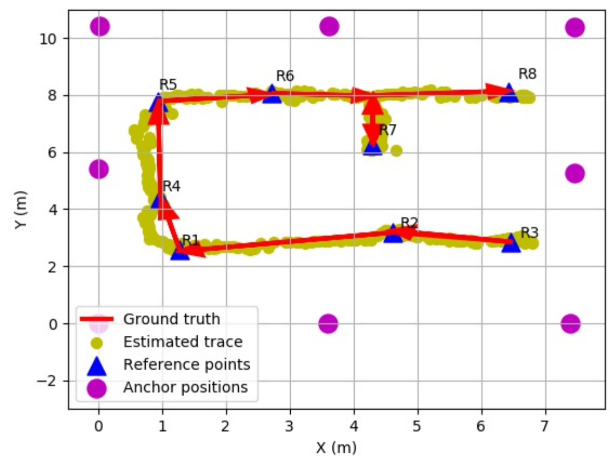

(a) Tag is moving in zigzag lines

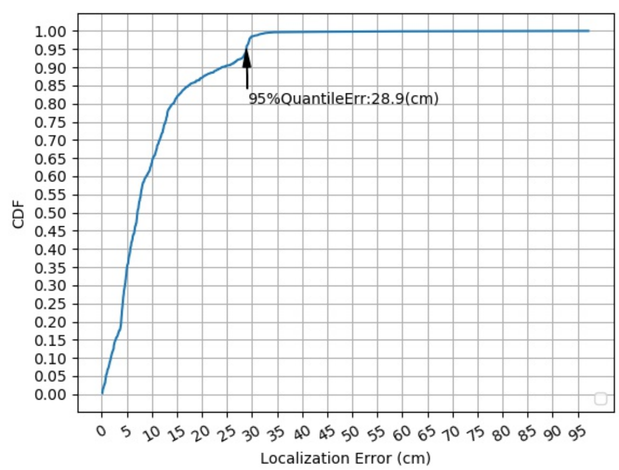

(b) The CDF of 2D localization error for zigzag trace pattern

Figure 6.13: Scatter plot and CDF of 2D dynamic localization results in the first testbed

addition, the orientation of the tag's antenna is set to be the best direction during stationary localization experiments, which is obviously impossible to optimize the facing of the tag's antenna during the tracking experiment.

Fig. 6.14 shows the 3D real time localization result from the second testbed.

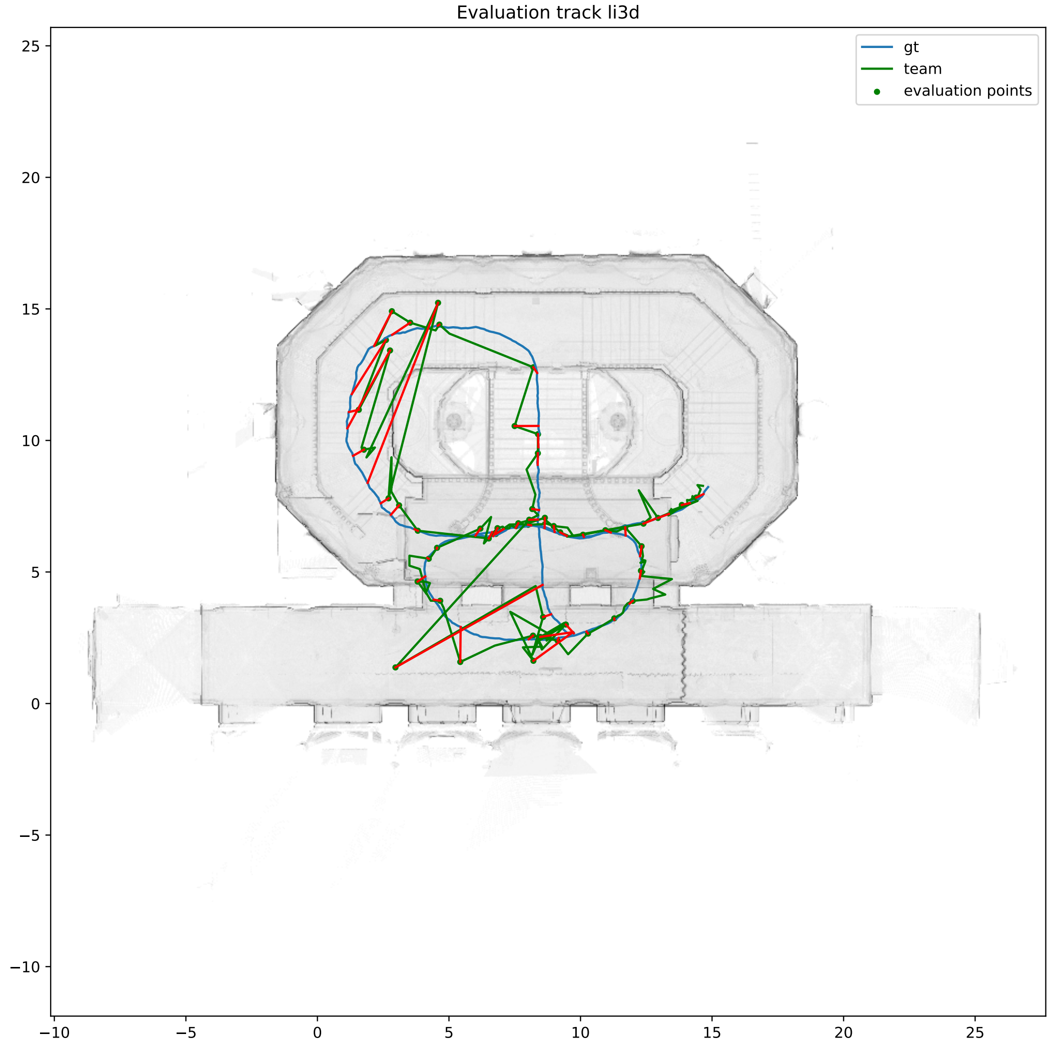

Figure 6.14: Scatters of 3D real time localization results in the second testbed

We were placed second out of five UWB-based only IPS teams with $0.92m$ average localization error [60]. The ground truth locations were measured using a backpack LiDAR equipment that can do simultaneous localization and mapping (SLAM) by the organizer. Such a relatively poor performance can be attributed to a number of reasons. First, the anchor locations are erroneous. Second, the anchor locations are not optimized. Third, after the competition, we found out only 75% locations were reported due to a software bug. Fourth, we did not apply the outlier detection method.

Chapter 7

Conclusion and Future Work

In this thesis, we proposed a low cost, real-time indoor positioning system based on commercial-off-the-shelf UWB transceivers. Experiments in two testbeds and ranging accuracy evaluation demonstrated the effectiveness of the proposed solution. There are nevertheless some limitations in the proposed system. Firstly, its scalability is restricted by means of the TMDS-TWR. Unlike the TDOA approach wherein tags only need to broadcast a single message for location estimation, TWR requires three messages between a tag and a specific anchor node, and multiple such exchanges are needed for one location fix. Even with optimization, at least $60ms$ is required to report a location. As the number of tags increases, if they operate in the same channel, a time division multiple access mechanism is needed to avoid congestions. This will significantly prolong the location update interval. Secondly, multi-sensor fusion is essential for improving localization performance in multipath rich environments. Although experiments demonstrated excellent performance in a lab environment, the accuracy in multipath rich environment is still low. As future work, we are interested in investigating fusion of IMU and UWB in indoor localization. Our board design can support multisensor fusion. Third, the UWB antenna is very sensitive. During testing, a slight angular adjustment could result in a $20cm$ ranging error. The UWB system could benefit from a proper omnidirectional antenna. Finally, the power consumption of the board is very high. This can be addressed by replacing WiFi with a BLE module, and reducing the rate of location fixes by incorporating IMU readings.

Bibliography

[1] D. Ltd. (2017) Dw1000 user manual v2.13. [Online]. Available: https://www.decawave.com/sites/default/files/dw1000_user_manual_2.13.pdf

[2] ——. (2014) Dwm1000 datasheet v1.6. [Online]. Available: https://www.decawave.com/sites/default/files/resources/DWM1000-Datasheet-V1.6.pdf

[3] B. Silva and G. P. Hancke, "Ir-uwb-based non-line-of-sight identification in harsh environments: Principles and challenges," *IEEE Transactions on Industrial Informatics*, vol. 12, no. 3, pp. 1188–1195, 2016.

[4] P. C. Ltd. (2013) Acs5200hfauwb datasheet. [Online]. Available: http://partron.co.kr/x.thums/product/f1ntOrk3Q5c.pdf

[5] STMicroelectronics. (2017) Stm32f105 datasheet. [Online]. Available: https://www.st.com/resource/en/datasheet/cd00220364.pdf

[6] L. Espressif Systems (Shanghai) Pte. (2018) Esp-wroom-02 datasheet. [Online]. Available: https://www.espressif.com/en/products/hardware/esp-wroom-02/resources

[7] B. A. Renfro, M. Stein, N. Boeker, and A. Terry, "An analysis of global positioning system (gps) standard positioning service (sps) performance for 2017," 2018.

[8] E. Kaplan and C. Hegarty, *Understanding GPS: principles and applications*. Artech house, 2005.

[9] Z. Sahinoglu, S. Gezici, and I. Guvenc, *Ultra-wideband positioning systems*. Cambridge university press Cambridge, UK:, 2008, vol. 2.

[10] A. Alarifi, A. Al-Salman, M. Alsaleh, A. Alnafessah, S. Al-Hadhrami, M. A. Al-Ammar, and H. S. Al-Khalifa, "Ultra wideband indoor positioning technologies: Analysis and recent advances," *Sensors*, vol. 16, no. 5, p. 707, 2016.

[11] H. Liu, H. Darabi, P. Banerjee, and J. Liu, "Survey of wireless indoor positioning techniques and systems," *IEEE Transactions on Systems, Man, and Cybernetics, Part C (Applications and Reviews)*, vol. 37, no. 6, pp. 1067–1080, 2007.

[12] L. Mainetti, L. Patrono, and I. Sergi, "A survey on indoor positioning systems," in *Software, Telecommunications and Computer Networks (SoftCOM), 2014 22nd International Conference on*. IEEE, 2014, pp. 111–120.

[13] J. Xiao, Z. Zhou, Y. Yi, and L. M. Ni, "A survey on wireless indoor localization from the device perspective," *ACM Computing Surveys (CSUR)*, vol. 49, no. 2, p. 25, 2016.

[14] S. He and S.-H. G. Chan, "Wi-fi fingerprint-based indoor positioning: Recent advances and comparisons," *IEEE Communications Surveys & Tutorials*, vol. 18, no. 1, pp. 466–490, 2016.

[15] microsoft indoor localization competition. (2017) ipsn. [Online]. Available: https://www.microsoft.com/en-us/research/event/microsoft-indoor-localization-competition-ipsn-2017/

[16] Y.-T. Wang, J. Li, R. Zheng, and D. Zhao, "Arabis: An asynchronous acoustic indoor positioning system for mobile devices," in *Indoor Positioning and Indoor Navigation (IPIN), 2017 International Conference on*. IEEE, 2017, pp. 1–8.

[17] F. C. Commission *et al.*, "First report and order, revision of part 15 of commissions rule regarding uwb transmission system fcc 02-48," *Washington, DC, April*, vol. 22, 2002.

[18] V. Sipal, B. Allen, and D. Edwards, "Impact of antennas on practical uwb signals," in *Antennas and Propagation (EuCAP), 2013 7th European Conference on*. IEEE, 2013, pp. 545–548.

[19] N. E. Klepeis, W. C. Nelson, W. R. Ott, J. P. Robinson, A. M. Tsang, P. Switzer, J. V. Behar, S. C. Hern, and W. H. Engelmann, "The national human activity pattern survey (nhaps): a resource for assessing exposure to environmental pollutants," *Journal of Exposure Science and Environmental Epidemiology*, vol. 11, no. 3, p. 231, 2001.

[20] technavio. (2016) Global indoor lbs market 2016-2020. [Online]. Available: https://www.technavio.com/report/global-machine-machine-m2m-and-connected-devices-global-indoor-lbs-market-2016-2020

[21] G. Shi and Y. Ming, "Survey of indoor positioning systems based on ultra-wideband (uwb) technology," in *Wireless Communications, Networking and Applications*. Springer, 2016, pp. 1269–1278.

[22] Z. Low, J. Cheong, C. Law, W. Ng, and Y. Lee, "Pulse detection algorithm for line-of-sight (los) uwb ranging applications," *IEEE Antennas and Wireless Propagation Letters*, vol. 4, no. 1, pp. 63–67, 2005.

[23] J. González, J.-L. Blanco, C. Galindo, A. Ortiz-de Galisteo, J.-A. Fernández-Madrigal, F. A. Moreno, and J. L. Martínez, "Mobile robot localization based on ultra-wide-band ranging: A particle filter approach," *Robotics and autonomous systems*, vol. 57, no. 5, pp. 496–507, 2009.

[24] I. TDC Acquisition Holdings. (2010) Timedomain website. [Online]. Available: https://timedomain.com/

[25] Y. Geng, J. He, and K. Pahlavan, "Modeling the effect of human body on toa based indoor human tracking," *International Journal of Wireless Information Networks*, vol. 20, no. 4, pp. 306–317, 2013.

[26] J. He, Y. Geng, and K. Pahlavan, "Toward accurate human tracking: Modeling time-of-arrival for wireless wearable sensors in multipath environment," *IEEE Sensors Journal*, vol. 14, no. 11, pp. 3996–4006, 2014.

[27] J. Tiemann, F. Eckermann, and C. Wietfeld, "Multi-user interference and wireless clock synchronization in tdoa-based uwb localization," in *Indoor Positioning and Indoor Navigation (IPIN), 2016 International Conference on*. IEEE, 2016, pp. 1–6.

[28] J. Tiemann and C. Wietfeld, "Scalable and precise multi-uav indoor navigation using tdoa-based uwb localization," in *Indoor Positioning and Indoor Navigation (IPIN), 2017 International Conference on*. IEEE, 2017, pp. 1–7.

[29] E. Fresk, K. Ödmark, and G. Nikolakopoulos, "Ultra wideband enabled inertial odometry for generic localization," *IFAC-PapersOnLine*, vol. 50, no. 1, pp. 11 465–11 472, 2017.

[30] N. Rajagopal, J. Miller, K. K. R. Kumar, A. Luong, and A. Rowe, "Welcome to my world: demystifying multi-user ar with the cloud: demo abstract," in *Proceedings of the 17th ACM/IEEE International Conference on Information Processing in Sensor Networks*. IEEE Press, 2018, pp. 146–147.

[31] J. Miller, N. Rajagopal, K. K. R. Kumar, A. Luong, and A. Rowe. (2018) Realty and reality: Where location matters. [Online]. Available: https://www.microsoft.com/en-us/research/uploads/prod/2017/12/John_Miller_2018.pdf

[32] U. Company. (2002) Ubisense website. [Online]. Available: http://www.ubisense.net/

[33] T. Phebey, "The ubisense assembly control solution for bmw," in *RTLS in Manufacturing Workshop-RFID Journal Europe Live*, 2010.

[34] A. Inc. (2006) Alereon website. [Online]. Available: http://www.alereon.com/

[35] B. W. Inc. (2011) Alereon announces breakthrough advances in uwb technology. [Online]. Available: https://www.businesswire.com/news/home/20111031005030/en/Alereon-Announces-Breakthrough-Advances-UWB-Technology

[36] D. Ltd. (2004) Decawave website. [Online]. Available: https://www.decawave.com/

[37] B. company. (2010) Bespoon website. [Online]. Available: http://www.bespoon.com

[38] A. R. Jiménez and F. Seco, "Comparing decawave and bespoon uwb location systems: Indoor/outdoor performance analysis," in *Indoor Positioning and Indoor Navigation (IPIN), 2016 International Conference on.* IEEE, 2016, pp. 1–8.

[39] A. R. J. Ruiz and F. S. Granja, "Comparing ubisense, bespoon, and decawave uwb location systems: Indoor performance analysis," *IEEE Transactions on instrumentation and Measurement*, vol. 66, no. 8, pp. 2106–2117, 2017.

[40] I. Pulse−LINK. (2000) Pulse−link website. [Online]. Available: http://www.pulselink.com/

[41] S. Gezici, Z. Tian, G. B. Giannakis, H. Kobayashi, A. F. Molisch, H. V. Poor, and Z. Sahinoglu, "Localization via ultra-wideband radios: a look at positioning aspects for future sensor networks," *IEEE signal processing magazine*, vol. 22, no. 4, pp. 70–84, 2005.

[42] H. T. Friis, "A note on a simple transmission formula," *Proceedings of the IRE*, vol. 34, no. 5, pp. 254–256, 1946.

[43] S. Marano, W. M. Gifford, H. Wymeersch, and M. Z. Win, "Nlos identification and mitigation for localization based on uwb experimental data," *IEEE Journal on Selected Areas in Communications*, vol. 28, no. 7, 2010.

[44] V. Savic, J. Ferrer-Coll, P. Ängskog, J. Chilo, P. Stenumgaard, and E. G. Larsson, "Measurement analysis and channel modeling for toa-based ranging in tunnels," *IEEE Transactions on Wireless Communications*, vol. 14, no. 1, pp. 456–467, 2015.

[45] A. G. Ferreira, D. Fernandes, A. P. Catarino, and J. L. Monteiro, "Performance analysis of toa-based positioning algorithms for static and dynamic targets with low ranging measurements," *Sensors*, vol. 17, no. 8, p. 1915, 2017.

[46] S. Leugner, M. Pelka, and H. Hellbrück, "Comparison of wired and wireless synchronization with clock drift compensation suited for u-tdoa localization," in *Positioning, Navigation and Communications (WPNC), 2016 13th Workshop on*. IEEE, 2016, pp. 1–4.

[47] K. Yu, I. Sharp, and Y. J. Guo, *Ground-based wireless positioning*. John Wiley & Sons, 2009, vol. 5.

[48] J. Kolakowski, A. Consoli, V. Djaja-Josko, J. Ayadi, L. Morrigia, and F. Piazza, "Uwb localization in eiger indoor/outdoor positioning system," in *Intelligent Data Acquisition and Advanced Computing Systems: Technology and Applications (IDAACS), 2015 IEEE 8th International Conference on*, vol. 2. IEEE, 2015, pp. 845–849.

[49] C. McElroy, D. Neirynck, and M. McLaughlin, "Comparison of wireless clock synchronization algorithms for indoor location systems," in *Communications Workshops (ICC), 2014 IEEE International Conference on*. IEEE, 2014, pp. 157–162.

[50] H. Matsumoto, H. Kusano, T. Morokuma, and K. Sakamura, "Numerical and experimental investigation of tdoa-based positioning system by ultra-wideband impulse radio," in *Wireless Sensors and Sensor Networks (WiSNet), 2011 IEEE Topical Conference on.* IEEE, 2011, pp. 25–28.

[51] V. Djaja-Josko and J. Kolakowski, "Uwb positioning system for elderly persons monitoring," in *Telecommunications Forum Telfor (TELFOR), 2015 23rd.* IEEE, 2015, pp. 169–172.

[52] M. L. Sichitiu and C. Veerarittiphan, "Simple, accurate time synchronization for wireless sensor networks," in *Wireless Communications and Networking, 2003. WCNC 2003. 2003 IEEE*, vol. 2. IEEE, 2003, pp. 1266–1273.

[53] D. Barclay, "Augmented reality with location tracking," Ph.D. dissertation, University of Manitoba, 2017.

[54] D. Ltd. (2014) Aps014: Antenna delay calibration of dw1000-based products and systems. [Online]. Available: https://www.decawave.com/sites/default/files/aps014-antennadelaycalibrationofdw1000-basedproductsandsystems_v1.01.pdf

[55] B. S. GmbH. (2018) Bmp280 datasheet. [Online]. Available: https://ae-bst.resource.bosch.com/media/_tech/media/datasheets/BST-BMP280-DS001-19.pdf

[56] I. . W. Group *et al.*, "Ieee standard for local and metropolitan area networkspart 15.4: Low-rate wireless personal area networks (lr-wpans)," *IEEE Std*, vol. 802, pp. 4–2011, 2011.

[57] D. Incorporated. (2013) Pam2305aab330 datasheet. [Online]. Available: https://www.diodes.com/assets/Datasheets/PAM2305.pdf

[58] D. Ltd. (2014) Aps017: Max range in dw1000 system. [Online]. Available: https://www.decawave.com/sites/default/files/aps017_max_range_in_dw1000_systems.pdf

[59] L. Geosystems. (2013) Leica disto s910 user manual. [Online]. Available: https://lasers.leica-geosystems.com/ca/sites/lasers.leica-geosystems.com.eu/files/leica_media/product_documents/disto/prod_docs_s910/leica-disto-s910-user-manual-805080-808183-806677-en.pdf

[60] M. I. L. Competition. (2018) Microsoft indoor localization competition official results announcement. [Online]. Available: https://www.microsoft.com/en-us/research/event/microsoft-indoor-localization-competition-ipsn-2018/